

Diversifying Composition Leads to Design Flexibility and Structural Fidelity in Blends

Le Ma^{1,2}, Hejin Huang³, Emma Vargo^{1,2}, Jingyu Huang¹, Christopher L. Anderson^{4,5},
Tiffany Chen^{2,4}, Ivan Kuzmenko⁶, Jan Ilavsky⁶, Cheng Wang⁷, Yi Liu⁵, Peter Ercius⁸,
Alfredo Alexander-Katz³ and Ting Xu^{1,2,4*}

¹Department of Materials Science and Engineering, University of California, Berkeley, CA 94720, USA

²Materials Sciences Division, Lawrence Berkeley National Laboratory, Berkeley, CA 94720, USA

³Department of Materials Science and Engineering, Massachusetts Institute of Technology, Cambridge, MA, 02139, USA

⁴Department of Chemistry, University of California, Berkeley, CA 94720, USA

⁵The Molecular Foundry, Lawrence Berkeley National Laboratory, Berkeley, CA 94720, USA

⁶Advanced Photon Source, Argonne National Laboratory, Argonne, IL 60439, USA

⁷Advanced Light Source, Lawrence Berkeley National Laboratory, Berkeley, CA 94720, USA

⁸National Center for Electron Microscopy, Molecular Foundry, Lawrence Berkeley National Laboratory, Berkeley, CA 94720, USA

*Corresponding author email: tingxu@berkeley.edu

Abstract:

In a blend of four or more components, the mixing entropy diversifies the chemical compositions of each phase. This reduces interfacial interactions, enhances inter-phase miscibility, weakens the dependence on specific pair interactions for self-assembly, and removes diffusion barriers to forming large-scale structures. When this design principle is applied to blends containing nanoparticles, colloidal particles, small molecules, and supramolecules, hierarchically-structured composites can be obtained with enhanced formulation flexibility in the filler selection and blend composition. Here, detailed characterization and simulations confirm entropy-driven phase behavior, where each component is distributed to locally mediate unfavorable interactions, and nanostructures form near or in a miscible state. Kinetically, this facilitates molecular diffusion across microdomains and through different phases, and ultimately leads to the facile fabrication of photonic crystals in minutes and nanocomposites with tunable microstructures. Besides advancing capabilities to engineer functional materials, the present study provides molecular insights into how entropy-driven complex blends navigate variations and uncertainties without compromising structural fidelity, as commonly seen in high-entropy alloys and biological blends.

Decades of efforts have been devoted to achieving hierarchical structures in simplified blends with parameterized components. However, in the case of organic/inorganic hybrids (1-4), it remains challenging to simultaneously modulate both nanostructures and microstructures to access properties seen in biological composites (5). Ordered arrays of nanoparticles are now routinely obtained using DNA (6, 7), supramolecules (8), block copolymers (BCPs) (9-11), polymer-grafted nanoparticles and/or via controlled evaporation/crystallization (12, 13). However, present successes almost exclusively rely on precise formulation with rather strict requirements as to the nanoparticle size, ligand chemistries, and nanostructures in host matrices (14-17), which significantly reduce their practicality outside of a test tube (1). More critically, there are inherent limitations on applying these precise approaches to control microstructures and beyond, where the lower-tier assemblies serve as the building blocks for the next tier. As the assembly proceeds, there is uncertainty as to when and where the next-tier building blocks form, and their size, shape and composition. The effects of unpredictable heterogeneities and variations are further amplified in macroscopic composites due to the large number of building blocks.

In contrast, biological blends form hierarchical assemblies with high fidelity and are able to accommodate fairly broad compositional variations/fluctuations (18, 19). Given that compositional complexity has been established as an important hallmark of biological blends and, more recently, high-entropy alloys (20), we reason that diversifying the variety of building blocks beyond ternary blends may enable entropy-driven phase behavior to accommodate unpredictable variations via system-wide cooperativity. **Fig. 1** schematically illustrates this concept when more components are added to a binary blend of polymers A

and B. The solubility parameters of all additive components are between those of polymers A and B, such that their dispersion in each phase mediates unfavorable A-B interactions. When only one component is added (i.e. a ternary blend), each phase has a defined composition but with an improved miscibility. When two or more types of components are added, the enhancement of the inter-phase miscibility is more pronounced. Furthermore, multiple composition combinations can give each phase the same cumulative chemical characteristics. It also becomes feasible to locally screen unfavorable interactions to disperse fillers, as shown in **Fig. 1B**. This opens a rarely-explored path to release current constraints in the composite design and to navigate uncertainties during structure formation over multiple length scales.

Experimentally, we apply this hypothesis to fabricate hierarchical composites by blending 4-7 components, including nanoparticles, colloidal particles, small molecules and coil-comb shaped supramolecules as detailed in **Fig.1C**. Three types of inorganic fillers are studied, ranging in size from 5 nm – 300 nm, and with respective ligand chemistries similar to polymer A, similar to polymer B, and chemically intermediate. Fe_3O_4 and NaYF_4 nanoparticles, 20 – 30 nm in size, are passivated with oleic acids. Silica particles, 100 nm - 300 nm in size, are covered by grafted polystyrene brushes, ~6-14 nm in thickness. These particles are synthesized in small scales with defined ligand chemistries. The third type of particle, zirconium oxide (ZrO_2) nanoparticles 4 - 6 nm in size, are sourced from a commercial vendor. The exact ligand composition is a trade secret, but NMR suggests a general alkyl-like chemistry (**Fig. S24**). The supramolecules, “PS-b-P4VP(PDP)₁”, are constructed from 3-pentadecyl phenol (PDP) hydrogen-bonding to the pyridyl side chains in polystyrene-block-poly(4-vinyl pyridine) (PS-b-P4VP) at a 1:1 molar ratio (21). Seven

small molecules or their isomeric mixtures are used, with solubility parameters between that of PS and P4VP(PDP)₁ (22, 23), including PDP, 3,5-Diiodo-dodecylbenzene (DID), 1,10-Decanediol dimethacrylate (DDMA), and four halogen-functionalized PDP molecules. Details of all blends tested are listed in **Fig.1C** and **Table S1**. The blends compositions use the following notation: supramolecule(SP)/particle size in nanometer/small molecules(SM:4VP molar ratio).

The size of nanoparticles determines their inherent properties and affects particle dispersion in polymers (9, 10, 14, 16, 24). Previous studies of nanostructured polymers showed that only fillers smaller than the matrix's feature sizes could be incorporated, in order to minimize polymer deformation and unfavorable filler/polymer interactions (9). This is consistent with observations of the S1/20 blend containing ~15-20 nm PS-rich and P4VP(PDP)₁-rich microdomains (**Fig. S1**): nanoparticles larger than 15 nm form large aggregates (**Fig. S2**). However, when any of the small molecule listed in **Fig. 1C** are added, this particle size constraint is eliminated. **Fig. 2A** show representative TEM images of the S1/20/PDP(1) blend (C1 in **Table S1**), with highly ordered nanoparticle arrays and distinct lamellar microdomains. Similar filler dispersion, though less inter-particle order, is obtained in blends with PS-grafted silica particles 100 - 300 nm in size. As shown in **Fig. 2B** and **Fig. S3**, the 100 nm silica particles are well-dispersed in S1/100/DID(2), and no filler aggregation is observed, though the particles are more than ~6 times larger than the microdomain width (100 nm vs. 15 nm). A zoomed-in TEM image in **Fig. 2A** confirms that oleic-acid passivated nanoparticles (20 nm) sit across both PS-rich and P4VP(PDP)₁-rich microdomains. In blends with the silica particles, the grafted PS layer also interfaces with both microdomains. Similar results are seen when the grafted PS-layer thickness is

varied. Thus, the interfaces between the fillers and each microdomain are effectively neutral, despite the different ligand chemistries. Furthermore, new morphologies appear in the organic matrix within the particle interstitials, such as woven structures reminiscent of interference patterns from wave propagation (**Fig. 2B**). These new morphologies contain abundant interfaces with high curvatures, suggesting that the energy cost to stabilize interfaces between the PS and P4VP(PDP)₁ microdomains is very low, or nonexistent. Thus, diversifying the blend composition effectively releases formulation constraints that previously limited the filler size and ligand chemistries that assembled into nanostructures. This is achieved by enhancing the blend's miscibility, minimizing energetic costs associated with interfaces, and eliminating the need to expel large particles, such that new morphologies locally emerge in response to particle incorporation.

To decipher the molecular origin of enhanced miscibility, we performed resonant soft X-ray scattering (RSOXS) (25, 26) and STEM-energy-dispersive X-ray spectroscopy (STEM-EDS). Different photon energies (280 eV, 285 eV and 286 eV) across the carbon 1s absorption edge were selected to decouple the scattering signal of the organic matrix from that of the nanoparticles in S1/20/PDP(1) (**Fig. 2C**). At photon energies below the carbon edge (280 eV), the scattering from nanoparticle dominates and the scattering pattern is similar to that seen in small angle X-ray scattering (SAXS). At the carbon edge (285 eV), resonant scattering from the PS and P4VP leads to intensified (001) and (002) diffraction spots (**Fig. 2C and 2D**), confirming the lamellar morphology in the matrix (**Fig. S7**). At 286 eV, the scattering pattern provides insights into the PDP distribution around the nanoparticles. By contrast-matching the rest of the organic matrix, fitted form factors show 20 nm nanoparticle cores with ~6 nm shells containing alkyl ligands and PDP. The

results indicate local enrichment of PDP surrounding the alkyl-passivated nanoparticles (**Fig. S7**).

STEM-EDS was used to image thin sections with edge-on lamellae to determine the small molecules' local distribution. An iodine-containing small molecule (DID) was used. In the STEM-EDS images of S1/20/DID(1) (C6 in **Table S1**), DID is clearly seen in the P4VP(PDP)₁-rich lamellae and in the areas surrounding nanoparticles in the PS-rich microdomain (**Fig. 2E and 2F**). The DID enrichment around the nanoparticles is consistent with the RSoXS results. The DID in the PS-rich lamellae mediates unfavorable interactions between particle ligands and both microdomains, as well as interactions between two microdomains. Thus, it is not energetically costly for the particles to span multiple microdomains and for the matrices to form new highly curved morphologies (27). Additional studies confirmed that the DID's spatial distribution varies depending on the particle size and the periodicity of supramolecule, but always leads to enhanced mixing (**Fig. S8**).

A coarse-grained simulation using dissipative particle dynamics (DPD) with a new parametrization force field (28) was carried out to probe the interplay among each component. A 4-component system was used containing a BCP with coil-comb structure to mimic the supramolecules, small molecules, and nanoparticles. Recent NMR studies confirmed the attachment of PDPs to the P4VP sidechains in the supramolecule, thus the use of coil-comb shaped BCP reflects experimental condition (29). The effect of intermolecular interactions on the nanoparticle ordering was examined using the interaction parameters listed in **Table S3**. When the pair interactions are representative of

the experimental conditions i.e. the interaction parameters of small molecules/coil block and small molecules/comb block are smaller than that of coil block/comb block, the nanoparticles spontaneously order into experimentally-observed assemblies: nanoparticles span across both microdomains, the small molecules are concentrated near the nanoparticles, and the small molecules are present in both microdomains (**Fig. 2G** and **2H**). The computation studies also informed two critical design rules to guide composite formulation. First, the small molecules need to have attractive interactions with nanoparticles. Neutral or repulsive filler/small molecule interactions lead to filler aggregation (**Fig. S9A**). Second, the comb architecture of the BCP is essential, because it produces long-range repulsion that compels the particles to order (**Fig. S9B**).

Thus, with increased number of ingredients, these composites self-adjust the spatial arrangement of each component to maximize inter-component miscibility to solubilize fillers. Under these conditions, it becomes feasible to form nanostructures when the blends are near or in a miscible state. Indeed, solution SAXS studies confirmed the formation of ordered nanoparticle assemblies in a SP1/20/PDP(1) containing 70-75 vol% good solvent (**Fig. 3A**). These new findings lead to a viable path to accelerate assembly kinetics by forming nanostructures in dilute solution, reducing viscosity and removing the enthalpic barrier to inter-microdomain diffusion. As a demonstration, rapid assemblies of composites based on a high molecular weight polymer, 330-b-125 kDa PS-b-P4VP, were tested. **Fig. 3B** and **3C** show a photonic crystal fabricated using S3/5/PDP(1) (C15 in **Table S1**) containing 9 vol% of 6 nm ZrO₂ nanoparticles. The TEM image shows a lamellar morphology with a periodicity of 143 nm, where alternating lamellae are 54 nm in thickness and densely packed with ZrO₂ nanoparticles (**Fig. S15**). In comparison to lengthy

assembly processes taking days (16, 30), complex blend-based photonic crystals are produced within 1 hour or less, overcoming a critical bottleneck for scalable fabrication. From a practical point of view, the ZrO₂ nanoparticles have an undefined surface chemistry. The successful and rapid fabrication of nanostructures demonstrated here clearly highlights the versatility of this approach.

Besides the particle size and surface chemistry, the formulation flexibility also applies to the small molecule chemistry and composition. When small molecules or their mixtures (listed in **Table S1**) are added, ordered arrays of nanoparticles form reproducibly (**Fig. S10**). The weight fraction of small molecules was varied between ~15 to ~42 wt%, corresponding to small molecule:4VP ratio between 0.5 to 1.5, without deleterious effects. When 4 different small molecules are added, similar nanoparticle assemblies were observed in the 7-component blends (**Fig. S10**). These results confirm the ability of these complex blends to accommodate a fairly broad range of compositional variations. However, when dodecyl succinic anhydride (DDSA) is added, large aggregates of particles form (**Fig. S11**). Thus, the small molecule's solubility parameter needs to be within those of PS and P4VP(PDP)₁, consistent with the design illustrated in **Fig. 1A**.

The resulting nanostructures are consistently reproducible with high uniformity, even with the formulation flexibility and enhanced miscibility. **Fig. 3D and 3E** show representative 3-D assemblies in S1/20/PDP(1). Based on high-angle annular dark-field scanning transmission electron microscopy (HAADF-STEM) tomography (31), the 3-D structure was determined to be a square lattice out-of-plane and hexagonal lattice in-plane as shown in **Fig. 3E (Movie S1)**. Statistical analysis (peak finding and lattice fitting; see **S3.2**) of nanoparticle unit cells confirmed a high level of structural uniformity (**Fig. 3F**,

Fig S5 and **Movie S2**) with the lattice parameters of $a = 51$ nm and $c = 32$ nm. This is consistent with SAXS profiles containing multiple orders of diffraction peaks, and also agrees with the morphology observed in the DPD simulation (**Fig. S6**). The simulation shows the same layered structure with in-plane hexagonal ordering, analogous to the hexatic B phase in liquid crystals. The particles from different layers are in registry, and the organic components are locally arranged with similar inter-layer registry in the PS-rich microdomain. This is different from the hexagonally-perforated layer morphology commonly seen in BCP, where the holes are out of registry (32). In simulation studies, when the nanoparticles are first arranged differently, they spontaneously return to the experimentally-observed ordered structures, suggesting that the assemblies are thermodynamically stable. (**Movie S4**).

The phase behavior of blends is predictable despite the compositional complexity, reflecting cooperative assemblies of all components. Composite libraries are studied to delineate contributions from each building block. As shown in **Fig. 3G**, the interlayer distance, c , is determined by the supramolecule molecular weight, and is ~ 31 nm for composites based on S1 (PS (33 kDa)-b-P4VP (8 kDa)PDP₁) and ~ 26 nm for that based on S2 (PS (19 kDa)-b-P4VP (5.2 kDa)PDP₁). The interlayer distance c remains near constant when the nanoparticle size is increased from ~ 15 nm to ~ 30 nm. The in-plane interparticle distance a is determined by both the nanoparticle size and the supramolecule (**Fig. 3H**). The edge-to-edge distance between two nanoparticles, d , is close to the microdomain size in supramolecule alone, independent of nanoparticle size (**Fig. 3H**). The experimental results are consistent with that from simulation. When comparing the morphology of particle-rich regions and no-particle regions in a PS layer with one row of particles

removed, the in-plane interparticle distance, d , increases as expected (**Fig. S12 and S13**). However, the lattice parameters of observed nanostructures have less dependence on small molecule chemistry and limited dependence on the small molecule composition. There is ~5% change in a and ~3% in c among all small molecules tested, where the nanoparticle size and small molecule-to-4VP stoichiometry are kept constant. When the PDP composition is varied from 15 wt% to 42 wt% in blends with fixed nanoparticle size, the overall change in a is within 12% , and within 3% for c (**Fig. 3I**). These results support the hypothesis that small molecules act as free agents and are distributed based on the needs to enhance miscibility, and reflect a system-level cooperativity and entropy-dominant phase behavior.

With high fidelity in nanostructure formation and sufficient molecular diffusion, it becomes thermodynamically and kinetically feasible to modulate higher-tier assemblies beyond nanostructures, a long-standing bottleneck preventing fabrication of hierarchical composites (33, 34). When the nanoparticle loading is below 8vol%, the composite separates into two phases, with and without nanoparticles, respectively (**Fig. S14**). Both experimental results and DPD simulation confirm the morphological change when the nanoparticles are incorporated. Experimentally, the presence of nanoparticles increases in-plane interparticle distance as shown in **Fig. 3H** and simulation results show a morphological transition from cylindrical morphology to a layered structure with in-plane hexagonally packed nanoparticles (**Fig.4A**). In either case, there is a geometric incompatibility such that the formation of nanostructures should lead to phase separation even without the presence of repulsive interactions. Ultra-small-angle X-ray scattering (USAXS) was carried out to simultaneously monitor the formation of nanostructure and

microstructure in composite solutions. **Fig. 4B** shows the merged USAXS and SAXS profiles of S1/20/PDP(1) as the solvent evaporates from a starting concentration of ~ 85 vol%. In the q -range of 0.0003 - 0.008 \AA^{-1} , a diffuse reflection appears at $q_{\text{max}} \sim 0.001 \text{ \AA}^{-1}$, increases in intensity at constant q_{max} and subsequently shift to lower q region. This USAXS profile evolution is consistent with the process of spinodal decomposition, with a characteristic fluctuation wavelength of ~ 600 nm, followed by the Ostwald ripening (35-37). Furthermore, the initiation of the long-range fluctuations coincides with the scattering intensity change at $q \sim 0.01 \text{ \AA}^{-1}$, corresponding to the early stage of nanostructure formation, indicating nanoscopic assemblies induce phase separation.

Fig. 4C-4F show the TEM images of C1 (S1/20/PDP(1)) with 5 vol % Fe_3O_4 nanoparticle loading. The morphology of microstructures is consistent with the USAXS results and suggests a spinodal decomposition process (37). The FFT analysis of TEM images shows the average correlation length of the microstructure is in the range of $1.2 \sim 3 \mu\text{m}$. In zoomed-in TEM images, ordered nanostructures are clearly seen in both particle-rich and no-particle phases and the interface between two phases is very sharp (**Fig. 4E and 4F**). When an external field, such as a magnetic field is applied, microstructures with elongated grains with high aspect ratios form with the long axis parallel to the field direction (**Fig. 4G-4I**), consistent with phase separation via a nucleation and growth process. When the SAXS and TEM results are compared, the nanoparticle assemblies are the same, and applied magnetic field only macroscopically aligns the assemblies as evidenced by many high order sharp reflections in the 2-D SAXS pattern (**Fig. 4H**).

Liquid cell TEM was used to locally visualize nanostructures during microstructure formation by entrapping the dilute solution of S1/20/PDP(1) (See **S3.1**). The solution phase

separated into two regions with different concentrations of nanoparticles, influenced by the conditions used to trap the solution (**Fig. S14A**). Within the nanoparticle-rich region, there is a characteristic inter-particle distance templated by the supramolecule although the order is poor. Worm-like nanostructures are also seen in the region without nanoparticles (Inset in **Fig. S14B**), confirming nanostructure formation in both phases. Given the sharp interfaces between the particle-rich and no-particle phases, the nanoparticles should have enough mobility to move across the structured organic matrix during the formation of microstructures.

Thus, by simply diversify a blend's composition, the mixing entropy gain provides energetic driving forces to form nanostructures in a miscible state that, subsequently, leads to subsequent phase separation. The resultant microstructures are similar to that of a binary polymer blends except each phase forms well defined nanostructures, validating a viable path toward hierarchically structured composites. The self-regulated spatial distribution of each component simultaneously provides the attractive interactions needed for nanoparticle incorporation, reduces preferential interactions to enhance phase mixing, and maximizes the system entropy. The blend is able to realize system-wide cooperativity to accommodate composition variations to form structures with high fidelity over multiple length scales. The quantitative analysis of each component's distribution, interactions between different phases, and the structural evolution pathway may also be valuable in understanding the rationale and critical role of complexity in natural systems, especially when it comes to the robustness needed to generate well-defined assemblies under constantly-changing conditions. Practically, this strategy significantly expands the range of possibilities for manipulating microstructures without compromising nanostructure

fidelity, and opens up processing windows to regulate composites based on the end needs of various technological sectors.

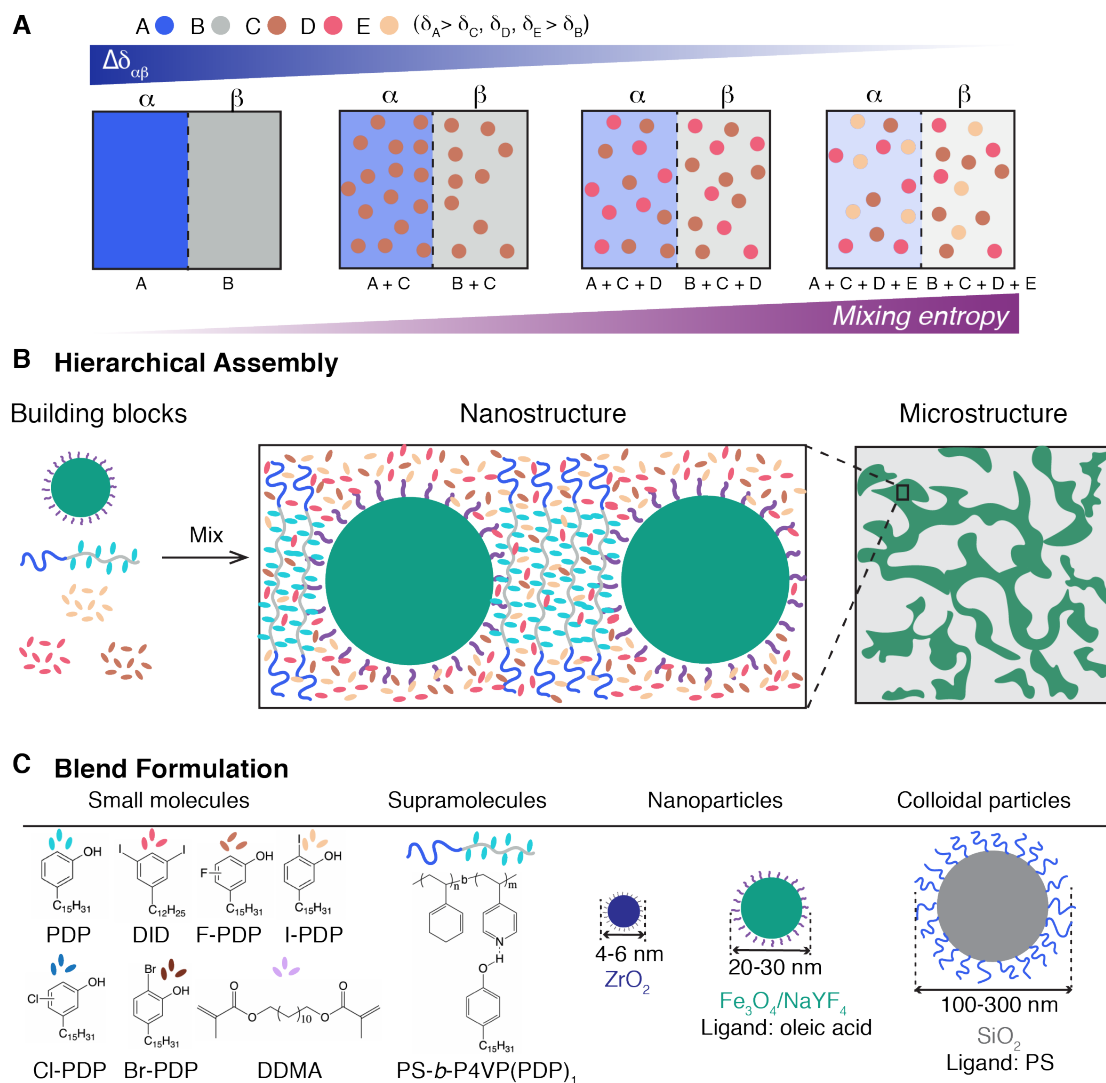


Fig. 1. Entropy-driven hierarchical assemblies in complex blends with design flexibility. **A**, Schematic of miscibility enhancement when additional components are added to an A-B binary polymer blend. The solubility parameters of all additive components (C-E) are between those of polymers A and B. α and β label the polymer A-rich and polymer B-rich phases, respectively. δ_i labels the solubility parameter of component i or phase i . $\Delta\delta_{\alpha\beta}$ is defined as $\delta_\alpha - \delta_\beta$, and indicates the immiscibility between phases α and β . **B**, Schematic of hierarchical assembly in the complex blends: molecular assembly, ordered nanostructure, and phase-separated microstructure. **C**, The blend ingredients used in the current studies including 7 organic small molecules, coil-comb supramolecules, and inorganic particles 5 nm to 300 nm in size with different ligand chemistries.

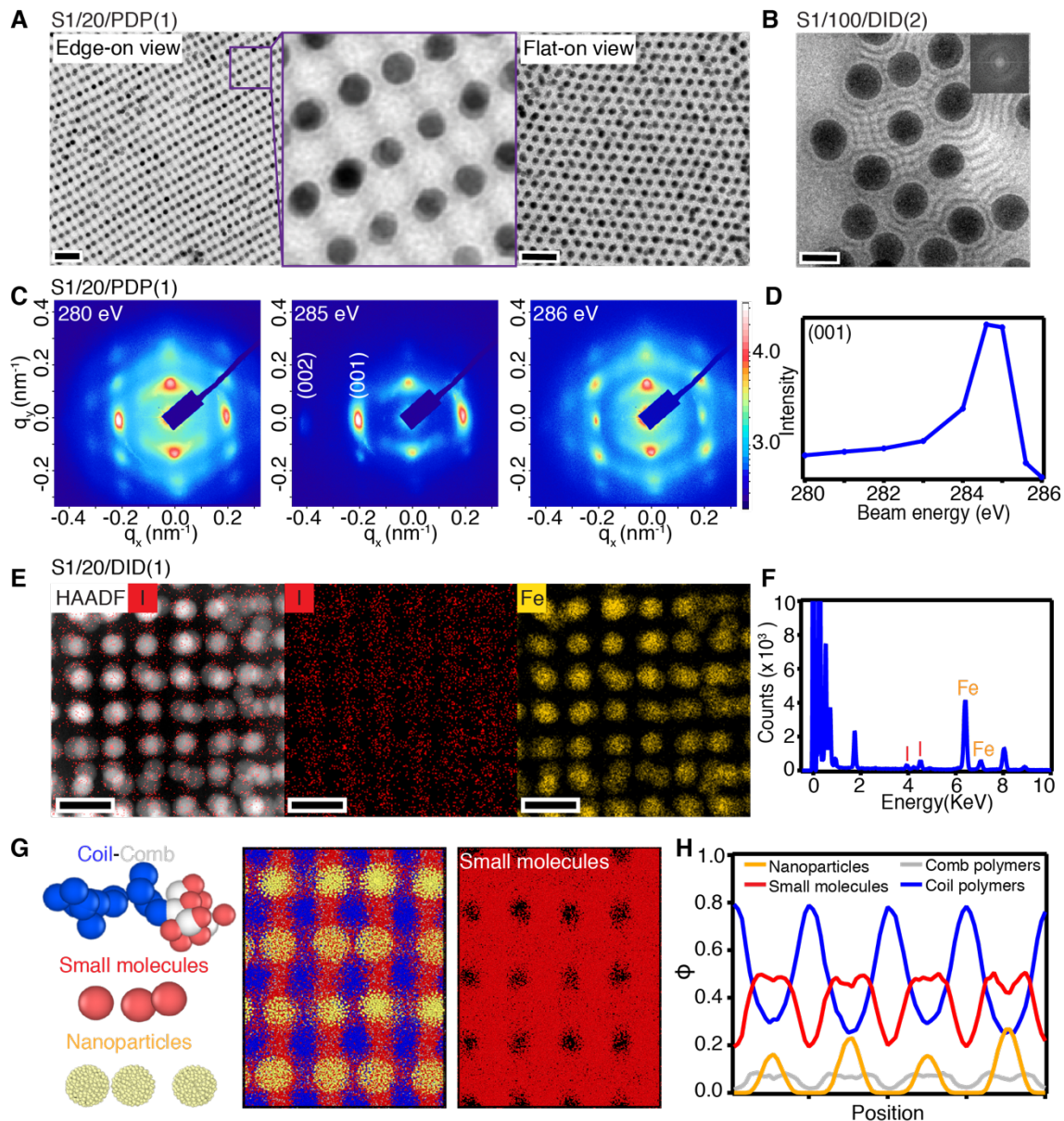


Fig. 2. Characterization and simulation of nanostructures in the complex blends. **A**, TEM images of C1 (S1/20/PDP(1)) forming highly-ordered nanoparticle arrays within an organic matrix forming lamellar morphology. The TEM images represent an edge-on and a flat-on view of the lamella, respectively. The center zoomed-in image is 150 nm \times 150 nm in size. **B**, TEM image of C14 (S1/100/DID(2)). The 100 nm PS-grafted silica particles are well-dispersed and co-assemble with the supramolecule and small molecules that form

woven structures at the interstitial sites among silica particles. The inset is the Fast Fourier Transform (FFT) of the image, showing the correlation between silica particles. **C**, 2-D RSoXS patterns of C1 at X-ray energies 280 eV, 285 eV, and 286 eV. **D**, Plot of (001) peak intensity as a function of X-ray energy, consistent with a lamellar morphology of the organic matrix. **E**, STEM-EDS maps of the element distribution in C6 (S1/20/DID(1)). The high-angle annular dark-field (HAADF) image shows the overall nanostructure. The I map indicates the distribution of iodine-labelled small molecules (red), and the Fe map shows the arrangement of nanoparticles (yellow). **F**, STEM-EDS spectrum of C6. **G**, DPD simulation results for a blend of coil-comb BCPs, small molecules, and nanoparticles. The morphology and component distribution are consistent with experimental results; the distribution of small molecules is highlighted. **H**, Density distribution profiles of each component in the coil polymer-rich block. **Scale bars: A, B** 100 nm. **E**, 50 nm.

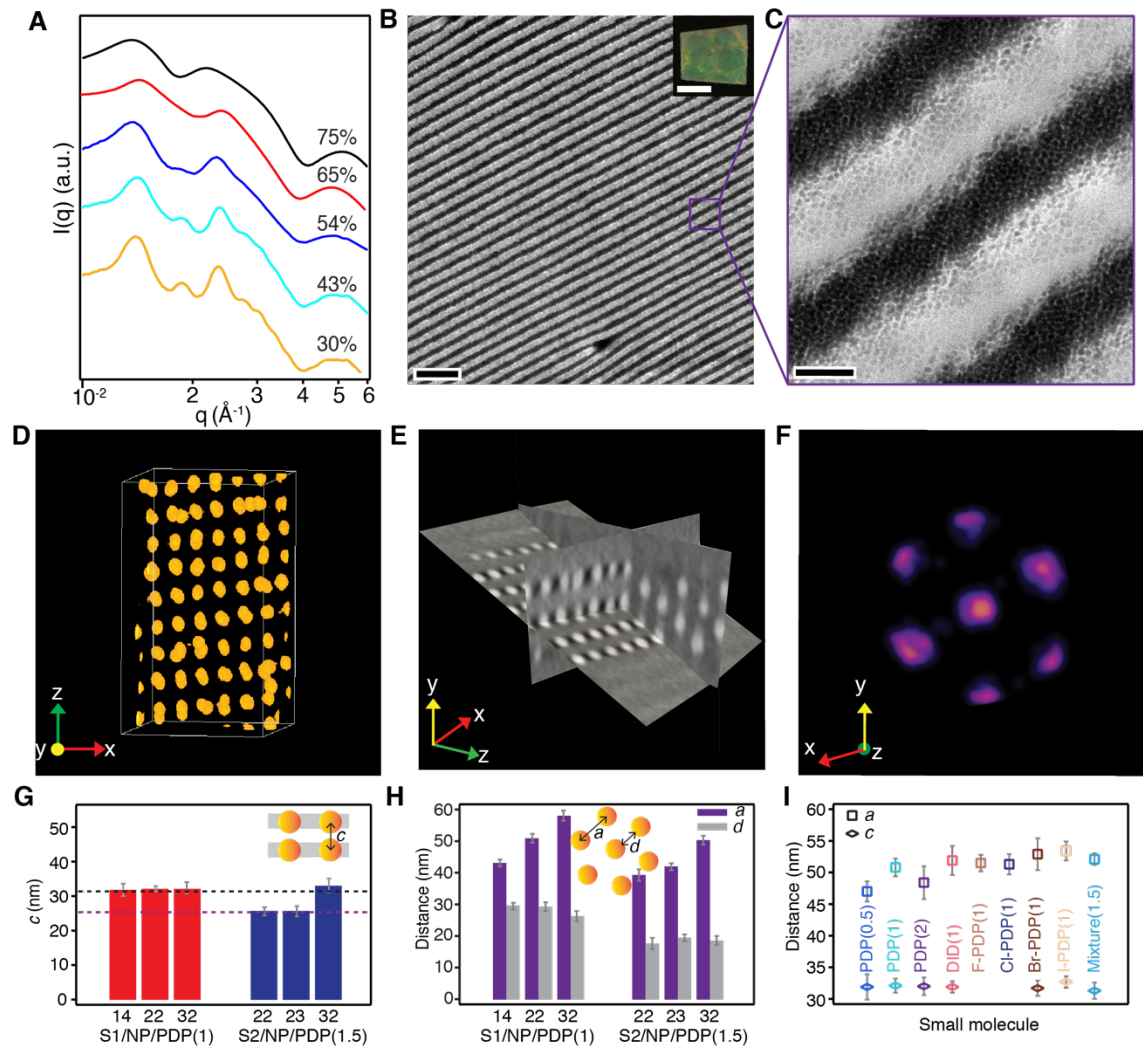


Fig. 3. Enhanced miscibility, fast assembly kinetics, formulation flexibility, and structural fidelity in complex blends. **A**, Solution SAXS profiles of C1 (S1/20/PDP(1)) as a function of solvent fraction. The solvent fraction is labelled on each profile, and the profiles are shifted vertically for clarity. **B**, **C**, TEM images of a photonic crystal produced by drying blend C15 (S3/5/PDP(1)) in < 1 hour from an initial solution with the solvent fraction of 85 vol%. The inset in **B** shows the iridescent green structural color produced by the photonic crystal. **D**, **E**, STEM tomography reconstruction of the blend C1, showing precise nanoparticle placement in 3-D. **D**, Tomography reconstruction of the nanoparticle arrangement, see also **Movie S1**. **E**, Three slices of the 3-D reconstruction; white dots are

nanoparticles. **F**, In-plane projection of the lattice unit cell averaged over ~ 200 unit cells. See also **Movie S2**. **G, H**, Plot of lattice parameter c (**G**), lattice parameter a and particle edge-to-edge distance d (**H**) in blends as a function of particle size and supramolecule composition. The number under the plot is the nanoparticle size (nm) for the corresponding bar. The black and purple dashed lines in **G** are the reference for the periodicity of S1 and S2 respectively. NP: nanoparticle. **I**, Plot of lattice parameters as a function of small molecule type and amount in S1/20/small molecules(SM:4VP molar ratio) blends. The mixture (1.5) is an abbreviation for DID (0.5)/F-PDP (0.5)/I-PDP (0.5). $n \geq 10$ measurements in **G, H, I** for each data point. **Scale bars: B**, 500 nm. **B inset**, 5 mm. **C**, 50 nm.

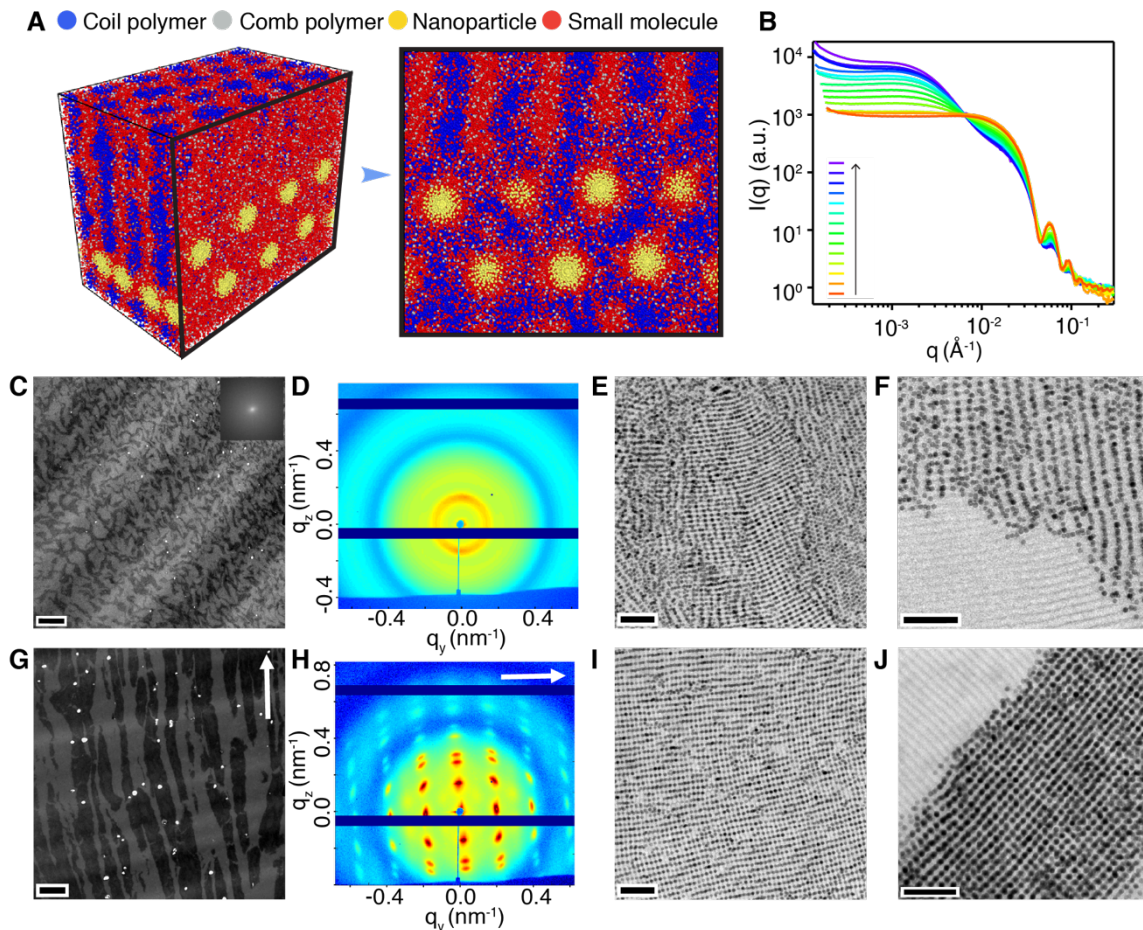


Fig.4. Hierarchical assemblies with ordered nanostructures and tunable microstructures. **A**, Results of a DPD simulation with decreased nanoparticle loading, showing the formation of particle-rich and no-particle regions. The second image is one projection of the 3D structure labeled by the black box. **B**, *In-situ* USAXS and SAXS profiles of C1 (S1/20/PDP(1)) as the solvent evaporated from ~85 vol% to ~80 vol% over 2 hours. The final solvent fraction was estimated using sealed calibration standards. The arrow direction indicates the drying process. **C-F**, TEM images and 2D SAXS pattern of C1 with 5 vol% Fe_3O_4 nanoparticles. The inset in **C** is the FFT of the image. **E** and **F** were taken at higher magnification to show the local nanostructure. **G-J**, TEM images and 2D SAXS pattern of C1 with 5 vol% Fe_3O_4 nanoparticles. The sample was dried within a magnetic field of ~0.1 Tesla (38), leading to macroscopic alignment. The arrows indicate

the magnetic field direction. **I** and **J** were taken at a higher magnification to show the local nanostructure. **Scale bars: C, G:5 μm . E, F, I, J: 200 nm.**

References:

1. S. K. Kumar, B. C. Benicewicz, R. A. Vaia, K. I. Winey, 50th anniversary perspective: are polymer nanocomposites practical for applications? *Macromolecules* **50**, 714-731 (2017).
2. C. Yi, Y. Yang, B. Liu, J. He, Z. Nie, Polymer-guided assembly of inorganic nanoparticles. *Chemical Society Reviews* **49**, 465-508 (2020).
3. Y. Wang, G. J. Desroches, R. J. Macfarlane, Ordered polymer composite materials: challenges and opportunities. *Nanoscale* **13**, 426-443 (2021).
4. A. C. Balazs, T. Emrick, T. P. Russell, Nanoparticle Polymer Composites: Where Two Small Worlds Meet. *Science* **314**, 1107-1110 (2006).
5. P. Fratzl, R. Weinkamer, Nature's hierarchical materials. *Progress in materials Science* **52**, 1263-1334 (2007).
6. M. R. Jones, N. C. Seeman, C. A. Mirkin, Programmable materials and the nature of the DNA bond. *Science* **347**, 1260901 (2015).
7. D. J. Lewis, L. Z. Zornberg, D. J. D. Carter, R. J. Macfarlane, Single-crystal Winterbottom constructions of nanoparticle superlattices. *Nature Materials* **19**, 719-724 (2020).
8. Y. Zhao *et al.*, Small-molecule-directed nanoparticle assembly towards stimuli-responsive nanocomposites. *Nature materials* **8**, 979 (2009).
9. M. R. Bockstaller, R. A. Mickiewicz, E. L. Thomas, Block copolymer nanocomposites: perspectives for tailored functional materials. *Advanced Materials* **17**, 1331-1349 (2005).
10. Y. Lin *et al.*, Self-directed self-assembly of nanoparticle/copolymer mixtures. *Nature* **434**, 55-59 (2005).
11. J. J. Chiu, B. J. Kim, E. J. Kramer, D. J. Pine, Control of nanoparticle location in block copolymers. *Journal of the American Chemical Society* **127**, 5036-5037 (2005).
12. X. Ye *et al.*, Structural diversity in binary superlattices self-assembled from polymer-grafted nanocrystals. *Nature Communications* **6**, 10052 (2015).
13. M. A. Boles, M. Engel, D. V. Talapin, Self-Assembly of Colloidal Nanocrystals: From Intricate Structures to Functional Materials. *Chemical Reviews* **116**, 11220-11289 (2016).
14. R. B. Thompson, V. V. Ginzburg, M. W. Matsen, A. C. Balazs, Predicting the Mesophases of Copolymer-Nanoparticle Composites. *Science* **292**, 2469-2472 (2001).
15. P. Akcora *et al.*, Anisotropic self-assembly of spherical polymer-grafted nanoparticles. *Nature materials* **8**, 354-359 (2009).
16. Y. Gai, Y. Lin, D.-P. Song, B. M. Yavitt, J. J. Watkins, Strong Ligand-Block Copolymer Interactions for Incorporation of Relatively Large Nanoparticles in Ordered Composites. *Macromolecules* **49**, 3352-3360 (2016).
17. S. G. Jang, E. J. Kramer, C. J. Hawker, Controlled supramolecular assembly of micelle-like gold nanoparticles in PS-b-P2VP diblock copolymers via hydrogen bonding. *Journal of the American Chemical Society* **133**, 16986-16996 (2011).
18. S. Boeynaems *et al.*, Protein phase separation: a new phase in cell biology. *Trends in cell biology* **28**, 420-435 (2018).

19. A. A. Hyman, C. A. Weber, F. Jülicher, Liquid-liquid phase separation in biology. *Annual review of cell and developmental biology* **30**, 39-58 (2014).
20. E. P. George, D. Raabe, R. O. Ritchie, High-entropy alloys. *Nature Reviews Materials* **4**, 515-534 (2019).
21. O. Ikkala, G. ten Brinke, Hierarchical self-assembly in polymeric complexes: towards functional materials. *Chemical Communications*, 2131-2137 (2004).
22. C. M. Hansen, *Hansen solubility parameters: a user's handbook*. (CRC press, 2002).
23. D. Van Krevelen, K. Te Nijenhuis. (Elsevier, Amsterdam, 2009).
24. M. R. Bockstaller, Y. Lapetnikov, S. Margel, E. L. Thomas, Size-selective organization of enthalpic compatibilized nanocrystals in ternary block copolymer/particle mixtures. *Journal of the American Chemical Society* **125**, 5276-5277 (2003).
25. C. Wang *et al.*, Defining the nanostructured morphology of triblock copolymers using resonant soft X-ray scattering. *Nano letters* **11**, 3906-3911 (2011).
26. F. Liu, M. A. Brady, C. Wang, Resonant soft X-ray scattering for polymer materials. *European Polymer Journal* **81**, 555-568 (2016).
27. L. Leibler, Theory of microphase separation in block copolymers. *Macromolecules* **13**, 1602-1617 (1980).
28. H. Huang, A. Alexander-Katz, Dissipative particle dynamics for directed self-assembly of block copolymers. *The Journal of chemical physics* **151**, 154905 (2019).
29. B. S. Chang, L. Ma, M. He, T. Xu, NMR Studies of Block Copolymer-Based Supramolecules in Solution. *ACS Macro Letters* **9**, 1060-1066 (2020).
30. W. Lee, J. Yoon, E. L. Thomas, H. Lee, Dynamic changes in structural color of a lamellar block copolymer photonic gel during solvent evaporation. *Macromolecules* **46**, 6528-6532 (2013).
31. P. Ercius, O. Alaidi, M. J. Rames, G. Ren, Electron tomography: a three-dimensional analytic tool for hard and soft materials research. *Advanced materials* **27**, 5638-5663 (2015).
32. I. Vukovic, G. ten Brinke, K. Loos, Hexagonally perforated layer morphology in PS-b-P4VP (PDP) supramolecules. *Macromolecules* **45**, 9409-9418 (2012).
33. M. Dalvi, C. Eastman, T. Lodge, Diffusion in microstructured block copolymers: Chain localization and entanglements. *Physical review letters* **71**, 2591 (1993).
34. M. Dalvi, T. Lodge, Parallel and perpendicular chain diffusion in a lamellar block copolymer. *Macromolecules* **26**, 859-861 (1993).
35. M. Rubinstein, R. H. Colby, *Polymer physics*. (Oxford university press New York, 2003), vol. 23.
36. J. W. Cahn, On spinodal decomposition. *Acta metallurgica* **9**, 795-801 (1961).
37. T. Hashimoto, M. Takenaka, T. Izumitani, Spontaneous pinning of domain growth during spinodal decomposition of off-critical polymer mixtures. *The Journal of chemical physics* **97**, 679-689 (1992).
38. Z. J. Urbach *et al.*, Probing the Consequences of Cubic Particle Shape and Applied Field on Colloidal Crystal Engineering with DNA. *Angewandte Chemie* **133**, 4111-4115 (2021).

39. S. Fischer, J. K. Swabeck, A. P. Alivisatos, Controlled Isotropic and Anisotropic Shell Growth in β -NaLnF₄ Nanocrystals Induced by Precursor Injection Rate. *Journal of the American Chemical Society* **139**, 12325-12332 (2017).
40. W. Stöber, A. Fink, E. Bohn, Controlled growth of monodisperse silica spheres in the micron size range. *Journal of colloid and interface science* **26**, 62-69 (1968).
41. W. Wei *et al.*, Observing the Growth of Pb₃O₄ Nanocrystals by in Situ Liquid Cell Transmission Electron Microscopy. *ACS applied materials & interfaces* **11**, 24478-24484 (2019).
42. J. Ilavsky, Nika: software for two-dimensional data reduction. *Journal of Applied Crystallography* **45**, 324-328 (2012).
43. E. Gann *et al.*, Soft x-ray scattering facility at the Advanced Light Source with real-time data processing and analysis. *Review of Scientific Instruments* **83**, 045110 (2012).
44. S. Förster, L. Apostol, W. Bras, Scatter: software for the analysis of nano-and mesoscale small-angle scattering. *Journal of Applied Crystallography* **43**, 639-646 (2010).
45. R. D. Groot, T. J. Madden, Dynamic simulation of diblock copolymer microphase separation. *The Journal of chemical physics* **108**, 8713-8724 (1998).
46. R. D. Groot, P. B. Warren, Dissipative particle dynamics: Bridging the gap between atomistic and mesoscopic simulation. *The Journal of chemical physics* **107**, 4423-4435 (1997).
47. J. Ilavsky *et al.*, Ultra-small-angle X-ray scattering instrument at the advanced photon source: history, recent development, and current status. *Metallurgical and Materials Transactions A* **44**, 68-76 (2013).
48. A. Arcadi, O. A. Attanasi, S. Berretta, G. Bianchi, P. Filippone, Synthesis of new cardanol derivatives through combined iodination/palladium-catalysed cross-coupling reactions. *Synthesis* **2006**, 2523-2530 (2006).
49. D. Felipe-Blanco, F. Alonso, J. C. Gonzalez-Gomez, Salicylic Acid-Catalyzed One-Pot Hydrodeamination of Aromatic Amines by tert-Butyl Nitrite in Tetrahydrofuran. *Advanced Synthesis & Catalysis* **359**, 2857-2863 (2017).
50. K. Cantin, S. Rondeau-Gagné, J. R. Néabo, M. Daigle, J.-F. Morin, H-Bonding-driven gel formation of a phenylacetylene macrocycle. *Organic & biomolecular chemistry* **9**, 4440-4443 (2011).

Acknowledgement: Funding: This work was funded by the U.S. Department of Energy, Office of Science, Office of Basic Energy Sciences, Materials Sciences and Engineering Division under Contract No. DE-AC02-05-CH11231 (Organic-Inorganic Nanocomposites KC3104). Scattering studies were done at the Advanced Light Source is supported by the U.S. Department of Energy, Office of Science, Office of Basic Energy Sciences, of the U.S. Department of Energy under Contract DE-AC02-05CH11231 and at Advanced Photon Source, use of the Advanced Photon Source was supported by the US Department of Energy, Office of Science, Office of Basic Energy Sciences, under Contract DE-AC02-06CH1135. A portion of this research used resources at the High Flux Isotope Laboratory, a DOE Office of Science User Facility operated by the Oak Ridge National Laboratory. We acknowledge the support of the National Institute of Standards and Technology, U.S. Department of Commerce, in providing the neutron research facilities used in this work. We thank P. Bai and Y. Xiao for initial sample preparation and measurements, J. Kwon for preparing the solution SAXS sample holder, X. Ye for synthesizing NaYF₄ nanoparticles, X. Zuo for SAXS measurement and K. Bustillo for EDS analysis. **Author contributions:** TX conceived the idea and guided the project. LM and EV performed studies contributed to Fig. 1, 2A-F, 3, and Fig. 4B-J. HH and AAK performed simulation in Fig.2G-H and 4a. TC synthesized PS-grafted silica nanoparticles. CLA and YL synthesized small molecules. PE performed tomography analysis. CW performed RSoXS data fitting. JI and IK performed USAXS experiments.

Data and Materials Availability: All data needed to evaluate the conclusions in the paper are present in the paper and/or the Supplementary Materials. For reproduction purposes,

raw data used to generate figures and input scripts used to produce the simulations are available on xxx.

Supplementary Materials for
Diversifying Composition Leads to Design Flexibility and Structural
Fidelity in Blends

Le Ma, Hejin Huang, Emma Vargo, Christopher L. Anderson, Tiffany Chen, Ivan
Kuzmenko, Jan Ilavsky, Cheng Wang, Yi Liu, Peter Ercius, Alfredo Alexander-Katz and

Ting Xu*

*Correspondence to: tingxu@berkeley.edu

This PDF file includes:

Materials and Methods
Figs. S1 to S23
Tables S1 to S6
Captions for Movies S1 to S4
References 39-50

Other Supplementary Materials for this manuscript include the following:

Movies S1 to S4

Materials and Methods

S1. Materials

PS (33 kDa)-*b*-P4VP (8 kDa) (PDI = 1.10), PS (19 kDa)-*b*-P4VP (5.2 kDa) (PDI = 1.10), PS (330 kDa)-*b*-P4VP (125 kDa) (PDI = 1.10) were purchased from Polymer Source, Inc. 3-*n*-Pentadecylphenol (PDP) (90%–95%) was purchased from ACROS Organics. Chloroform was purchased from Fisher Scientific, and no HCl was detected using NMR. Iron oxide nanoparticles with core sizes of 15 nm, 20 nm, 25 nm, and 30 nm were purchased from Ocean Nanotech. NaYF₄ nanoparticles were synthesized using the method provided by Paul Alivisatos's group (39). PS-grafted silica nanoparticles were synthesized using the method provided in **S1.1**. ZrO₂ nanoparticle with core size of 4-6 nm was purchased from pixelligent. The exact surface chemistry is a trade secret, but an NMR spectrum is provided in **Fig. S23**. The Detailed information for the nanoparticles is in **Table S2**.

Deuterated solvents were purchased from Cambridge Isotope Laboratories and used as received. All other commercially-available chemicals were purchased from Alfa Aesar, Spectrum Chemicals, Acros Organics, TCI America, or Sigma-Aldrich and were used without further purification. A number of halogenated alkylphenols were synthesized from PDP; however, the lighter halogens (chloro- and fluoro-substituted) produced mixtures of isomers, which could not be easily purified from each other. 2-iodo-5-pentadecylphenol (I-PDP) was synthesized from PDP in one step via reaction with molecular iodine in the presence of potassium iodate. 2-bromo-5-pentadecylphenol (Br-PDP) was synthesized from PDP with N-bromosuccinimide in chloroform in the presence of acetic acid. Isomers of monochloro-pentadecylphenol were synthesized from PDP in 1,1,2-trichloroethylene with N-chlorosuccinimide in the presence of acetic acid. Isomers

of monofluoro-pentadecylphenol were synthesized from 3-pentadecylphenol with selectfluor. Additionally, 3,5-diiodo-dodecylbenzene (DID) was synthesized from 4-dodecylaniline in two steps. First, the aniline was iodinated with pyridine iodine monochloride; then, the amine group was removed under modified Sandmeyer conditions. Detailed synthesis information is provided in S8 (Fig. S16-22).

S1.1 Silica nanoparticle synthesis

S1.1.1 PS-grafted silica nanoparticles synthesis

Chemicals were purchased from Sigma Aldrich and Fisher Scientific unless stated otherwise. Azobisisobutyronitrile (AIBN) was recrystallized in ethanol prior to use. Styrene (99%) was purified by passing through a short column of basic alumina to remove the inhibitor.

S1.1.2 Synthesis of amino functionalized silica nanoparticles

Silica nanoparticles (SiO₂ nanoparticles) were synthesized by the Stöber method (40). Ethanol (11.7 mL), deionized water (10.6 mL) and tetraethyl orthosilicate (TEOS, 99.9%, 0.5 mL) were mixed in a flask and stirred for 10 min. Ammonium hydroxide (28%, 10 mL) was added dropwise to catalyze the condensation reaction. The reaction continued for 1 h at 20 °C. The SiO₂ nanoparticles in the white turbid suspension were collected by centrifugation at 7000 rpm for 5 min. The particles were washed three times with ethanol and water. The SiO₂ nanoparticles were then dispersed in ethanol under ultrasonication. (3-aminopropyl) triethoxysilane (APTES, 0.2 mL) was added to the solution and the reaction mixture was stirred at 20 °C for 24 h. Amino-functionalized SiO₂ nanoparticles were washed with ethanol three times and recovered by centrifugation at 7000 rpm for 10 min.

S1.1.3 Synthesis of RAFT agent immobilized silica nanoparticles

Amino-functionalized SiO₂ nanoparticles were dispersed in *N,N*-dimethylformamide (DMF, 2 mL) by ultrasonication. 2-(Dodecylthiocarbonothioylthio)-2-methylpropionic acid *N*-hydroxysuccinimide ester (20 mg) was added to the suspension. The reaction was stirred at 20 °C for 24 h. RAFT agent immobilized SiO₂ nanoparticles were washed with DMF three times and recovered by centrifugation at 7000 rpm for 10 min.

S1.1.4 RAFT polymerization of styrene using RAFT agent immobilized silica nanoparticles

AIBN (20.0 mg, 0.12 mmol) was dissolved in 1 mL of DMF. Styrene (2.08 g, 20 mmol), AIBN solution (0.165 mL, 0.02 mmol of AIBN), and RAFT agent immobilized silica nanoparticles (suspension in 1 mL of DMF) were mixed in a 20 mL vial. The solution was degassed with nitrogen for 20 min. The vial containing the reaction mixture was immersed in an oil bath and heated to 70 °C for 24 h. After the reaction, polystyrene-grafted SiO₂ nanoparticles were washed with DMF three times and recovered by centrifugation at 7000 rpm for 10 min.

S2. Sample preparation

PS-*b*-P4VP(PDP)₁ was first dissolved in chloroform to form a 15 mg/ml solution. The desired amounts of small molecules were added to the solution and stirred overnight. Details of all blend compositions are listed in **Table S1**. Nanoparticle suspensions were then mixed with solutions of polymer and small molecules. Details of all nanoparticles are listed in **Table S2**. The ratio of the nanoparticle solution to the polymer/small molecule solution was controlled to reach the desired nanoparticle loading. The solution samples

were directly used for solution scattering experiments. To prepare the bulk samples, ~ 300 μL of the blend solution was dried in a Teflon beaker at room temperature until ~40 μL (the solvent fraction is ~80%) of the solution remained. The solution was transferred to a small chamber, which caused the solvent to evaporate slowly, and dried overnight.

The photonic crystal sample was prepared as described above, but the solution was never transferred to the small chamber. Instead, 250 μL of blend solution was fully dried from an initial solvent fraction of 85%. The Teflon beaker was left uncovered, and fanned to increase the solvent evaporation rate. The rough white surface of the beaker strongly scattered light, so the experiment was repeated in a glass vial to monitor the color during drying (**Fig. S15**).

For magnetic field alignment, a ~0.1 Tesla magnetic field was applied to the small chamber (0.06-inch thickness) during solvent evaporation by using three 1/2-inch \times 1/8-inch neodymium rare earth disc magnets on each side. As before, the solvent slowly evaporated overnight.

S3. Morphology characterization

S3.1 Transmission electron microscopy (TEM)

Samples were embedded in resin (Araldite 502, Electron Microscopy Sciences) and cured at 60 $^{\circ}\text{C}$ overnight. Sections about 60 nm in thickness were microtomed using an RMC MT-X Ultramicrotome (Boeckler Instruments), floated on top of water, and picked up on copper TEM grids. If needed, samples were stained with iodine vapor to selectively stain the P4VP region. The thin sections were imaged using a FEI Tecnai 12 at an accelerating voltage of 120 kV. For liquid cell TEM, the solution was entrapped in a

homemade liquid TEM cell made with two TEM grids (41). **Fig. S1** shows different morphologies of BCP/small molecule blends. **Fig. S2** shows the morphology of the blend (S1/20) without free small molecules. **Fig. S3** and **Fig. S4** show morphologies of blends containing PS-grafted silica particles.

S.3.2 High-angle annular dark-field scanning transmission electron microscopy (HAADF-STEM) tomography

The projection images for 3D electron tomography were collected using a FEI TitanX 60-300 microscope with a 10 mrad probe semi-convergence angle operated at 200 kV at the National Center for Electron Microscopy (NCEM) facility of the Molecular Foundry. The pixel size was 4.76 nm. A hummingbird heavy tomography holder was used to acquire a series of TEM images at tilt angles ranging $\pm 70^\circ$ at an angular interval of 1° . The tilt series were aligned and reconstructed using the eTomo software of the IMOD tomography package. Reconstruction was done using the weighted-back-projection method. 3D visualization was performed using Tomviz 1.3.1. Through the reconstruction (**Fig. S5**), slices show the nanoparticles as white dots, and black dots are common artifacts of the reconstruction process due to the missing information in the acquired data (the missing wedge). Peak fitting and statistical methods were used to analyze the superlattice's unit cell formed in the multicomponent system. First, each nanoparticle's position is determined using peak finding and 3D Gaussian fitting based on the intensity of the tomography reconstruction. A local lattice fit was then performed to determine the unit cell parameters (a , b , c , α , β , γ). The parameters of this local lattice match the ensemble measurements from SAXS data. For each nanoparticle, the 1-8 nearest neighbors and their distances are calculated. **Fig. S5I** shows the distance distribution histogram of these nearest

neighbors. Finally, all nanoparticles centers are assigned to position (0, 0, 0) and all surrounding neighbors are plotted together. This plot shows the superlattice unit cell and indicates how dispersed the nanoparticles are in terms of their lattice positions (**Fig. S5J**).

S3.3 Small-angle X-ray Scattering (SAXS)

SAXS experiments were performed at beamline 8-ID-E and 12-ID-B at Advanced Photon Source (APS) at Argonne National Laboratory and beamline 7.3.3 at Advanced Light Source (ALS) at Lawrence Berkeley National Laboratory. The X-ray wavelengths are 1.13 Å at 8-ID-E, 0.93 Å at 12-ID-B and 1.24 Å at 7.33. The scattered X-ray intensity distribution was detected using a high-speed detector: Pilatus 1M at 8-ID-E, and Pilatus 2M at 12-ID-B and 7.3.3. The SAXS experiment with the applied magnet field was performed at beamline 12-ID-B (32). Images were plotted as intensity (I) vs q , where $q = (4\pi/\lambda) \sin(\theta)$, λ is the wavelength of the incident X-ray beam, and 2θ is the scattering angle. The sector-average profiles of SAXS patterns were extracted using Igor Pro with the Nika package (42). **Fig. S6** shows the 1D circular-averaged SAXS profiles of the blend C1(S1/20/PDP(1)).

S4. Composition distribution analysis

S4.1 Resonant soft X-ray scattering (RSoXS)

RSoXS experiments were performed at beamline 11.0.1.2 at the Advanced Light Source at Lawrence Berkeley National Laboratory (43). The samples were macroscopically aligned via a ~0.1 Tesla magnetic field and microtomed to 100 nm before deposition onto the Silicon Nitride membranes (Norcarda) with a 100 nm membrane thickness, 1 mm × 1 mm window size, and 5 mm × 5 mm frame size. The soft X-ray scattering data were

collected in a transmission geometry with an in-vacuum CCD camera. Multiple X-ray energies were selected, and the data was reduced using the Nika software package with a custom plugin. Scattering simulation was done using Scatter (44). A 2D rectangular lattice with unit cell dimensions ($a = 51$ nm, $b = 32$ nm, $\gamma = 90^\circ$) was chosen to represent the 001 projection of the nanoparticle array. A core-shell spherical form factor was used to represent the core shell nanoparticle with a homogeneous Fe_3O_4 core of 20 nm diameter ($R_c = 10$ nm) and homogenous PDP shell of 6 nm ($R_s = 16$ nm), with a relative standard deviation $\sigma = 0.25$ nm. 2D simulation was conducted assuming a single crystal projection with average domain size of 400 nm and a Debye-Waller factor, for the average displacement from the ideal lattice, of 5 nm. A Gaussian peak shape was applied for the Bragg peaks. For the lamellae simulation, a 32 nm pitch was used. This simulation serves as a qualitative representation of the RSoXS results, because it's limited by several factors, including the software capabilities and the complexity of mixing multiple phases. The Scatter program doesn't support energy-dependent resonant optical properties, so we opted to vary the ratio of the effective electron density between the core, the shell, and the matrix to emulate the optical constant variation as a function of photon energy. This is reflected in the significant scattering peak intensity change as the core-shell form factor goes through resonant energies. Thus, our conclusions are based on the scattering peak intensity variation with matching/mismatching effective electron density between the core-shell and matrix. Simulation results were seen in **Fig. S7**.

S4.2 STEM-energy dispersive X-ray spectroscopy (STEM-EDS)

STEM-EDS was performed at NCEM by using a FEI TitanX 60-300 microscope operated at 200 kV. The Bruker windowless EDS detector with a solid angle of 0.7

steradians enables high count rates with minimal dead time. The data were visualized with Esprit 1.9. **Fig. S8** shows the EDS maps of the complex blends with different compositions.

S5. Dissipative particle dynamics (DPD) simulation

The simulation method used in this paper is called Dissipative Particle Dynamics (DPD), which is a coarse-grain Molecular Dynamics. The setup of DPD is modified from the previously reported DPD method (45). In this simulation, there are four different types of beads (A, B, C, and D), which represent comb polymer (P4VP), coil polymer (PS), nanoparticle, and small molecule (PDP) respectively. Each PS-b-P4VP polymer is represented by 20 beads, composed of A type (which represents P4VP) and B type (which represents PS). The beads within the same polymer are interconnected in a linear fashion by a harmonic bond. The force field of the harmonic bond between two beads, i and j, is given by:

$$F_{i,j}^{bond} = K(r_{i,j} - r_0)\hat{r}_{ij} \quad (1)$$

In equation (1), the K is the spring constant while r_0 is equilibrium distance.

In the experiment, approximately half of the PDP forms a hydrogen bond with a P4VP monomer to form the bottlebrush architecture of the P4VP subchain. This is represented by attaching three individual PDP beads to each P4VP bead through a harmonic bond in the simulation (the ratio 3:1 between H-bonded PDP and P4VP is approximated by the volume ratio between each PDP molecule and P4VP monomer). Other than the bonded PDP, there is also an equal amount of free PDP beads in the simulation, which represents the excess PDP.

The last category of beads is the nanoparticles. Each nanoparticle is represented by 624 beads arranged densely in a spherical shape and interconnected by bonds with restricted bond distance and angle. During the simulation, all 624 beads move together with the same velocity because of this bonding. The nanoparticle has a radius of 3.0, and the density of beads inside the nanoparticle is 6.0. No BCP or PDP is allowed to penetrate into the nanoparticles because of its high density and its larger repulsive force (the interaction is double between nanoparticle and other beads). The mass of each nanoparticle is approximately 6.2×10^4 . The size and the mass of each nanoparticle are based on the experimental values.

In the DPD simulation, a soft repulsive force exists between two random beads that are close to each other. This force is defined by the equation:

$$F_{ij}^C = \begin{cases} -a_{ij}(1 - |r_{ij}|)\hat{r}_{ij} & \text{if } |r_{ij}| < 1 \\ 0 & \text{if } |r_{ij}| \geq 1 \end{cases} \quad (2)$$

In equation (2), a_{ij} represents the maximum repulsion between particle i and particle j , and r_{ij} is the distance between the two particles. Based on previously-reported literature, the repulsion parameter for the same particle is (45, 46):

$$a_{ii}\rho = 75kT \quad (3)$$

where ρ is the bead density, k is the Boltzmann constant, and T is the temperature. In our simulation, we choose the density to be $\rho = 5$, which gives $a_{ii} = 15kT$. The Flory-Huggins parameters χ between two different species is mapped to the repulsion parameter by the equation (4):

$$a_{ij} \approx a_{ii} + 1.45\chi_{ij} \quad (4)$$

Besides the soft repulsive potential, two other forces are thermal fluctuation and drag force.

These two forces are defined by the equation:

$$F_{ij}^R = \sigma w^R(r_{ij}) \theta_{ij} \hat{r}_{ij} \zeta / \sqrt{\delta t} \quad (5)$$

$$F_{ij}^D = \frac{1}{2} \sigma^2 \left(w^R(r_{ij}) \right)^2 / kT (v_{ij} \cdot \hat{r}_{ij}) \hat{r}_{ij} \quad (6)$$

The ζ in equation (5) is a random variable with zero mean and variance one, and $w(r) = (1 - r)$ for $r < 1$ and $w = 0$ for $r > 1$.

We use reduced units in the DPD simulation: thermal energy kT is set to 1 while the mass of bead A, B and D is unit mass (1.0). Bead type C, which represents nanoparticles, has a much larger mass (100.0). In this paper, all simulations were run for at least 1,000,000 time steps while the time step (Δt) is set to 0.015. Furthermore, three critical parameters of the above equations are fixed: $K = 50$, $r_0 = 1.0$ and $\sigma = 0.10$. According to the previous literature (38, 39), these settings give an excellent description of a 20-beads BCP system. The size of the simulation box is $46.1 \times 28.8 \times 39.9$. These length scales are chosen based on the periodicity of the self-assembled nanocomposite. There are 64 nanoparticles, 5200 BCP chains, and 124800 PDP particles (half of them are H-bonded and half are free) in the simulation.

The main parameter varied in this simulation is a_{ij} , which is set based on the chemical incompatibility between two different species in equation (6). The detailed parameter information is shown in **Table S3**. For interactions between nanoparticles and other species, the repulsive parameter a_{ij} has been scaled up by a factor of 2 in order to prevent penetration of other particles into the nanoparticles. $a_{AC} = a_{CC} = 30$ represents neutral condition (that is, $\chi = 0$) while $a_{CD} < 20$ and $a_{BC} = 35.8$ represent attractive ($\chi < 0$) and repulsive interaction ($\chi > 0$) between the two species, respectively. The simulation consists of two steps: 1. the positions of the nanoparticles are fixed to have the same particle arrangement as the equilibrium state in this step, while the coil-comb BCP and small

molecules can move freely based on the intermolecular interaction; 2. the positions of the nanoparticles are unfixed, and all the four components of the system move based on the intermolecular interactions (**Movie S3**). Because of the time scale of the experiment, the DPD simulation is incapable of simulating the system from a completely random state. Therefore, in Step 1, by fixing the nanoparticles, we gained insight into how the BCP and PDP co-assemble to minimize the free energy of the system when the nanoparticles have a fixed symmetry. In step 2, the positions of nanoparticles are released to ensure that the system is at equilibrium. Simulations have also been performed with the positions of the nanoparticles away from equilibrium, but they gradually recover to the six-fold symmetry (the structure observed in the experiment), as shown in **Movie S4**. Each simulation step has a relaxation period of 1,000,000 time steps. **Fig. S9** shows the DPD simulation results with various intermolecular interactions in complex blends.

S6. Formulation flexibility and nanostructure fidelity in complex blends

The composites show a high degree of flexibility in their formulation and can accommodate many formulation variations without compromising their nanoscopic order. Well-ordered, uniform assemblies are obtained in complex blends with varied nanoparticle core chemistry, nanoparticle size, supramolecule composition, small molecule type, and small molecule amounts (**Fig. S10**). **Table S4** lists the lattice parameter as a function of particle size and supramolecule type. **Table S5** lists the lattice parameter as a function of small molecule type and amount. The lattice parameters were measured based on TEM images using Image J. At least 10 different unit cells are measured for each sample. There are requirements for flexibility: the Flory-Huggins parameters of small molecules/PS block

and small molecules/P4VP(PDP)₁ block are smaller than that of PS/P4VP(PDP)₁. The Flory-Huggins parameters were calculated based on the solubility parameter of each component and the results are shown in **Table S6** (22, 23, 35). All small molecules listed in the **Table S6** meet the requirement except dodecyl succinic anhydride (DDSA). Therefore, when DDSA is added, large aggregates of particles form (**Fig. S11**).

For ordered lattices, the interlayer distance c is mainly set by the microdomain size of the supramolecule, and the in-plane interparticle distance a is determined by both the particle size and the microdomain size of the supramolecule. The experimental results are consistent with the simulation. Each PS layer is arranged in a perforated lamellae (PL) structure. Assuming that there are no nanoparticles inside the PL phase, the distance between the holes of the PL will be equivalent to the domain size, eg. $d = 32$ nm for S1. The inclusion of nanoparticles makes the in-plane periodicity $2\Delta a$ larger, as shown in **Fig. S12B**, where Δa is the radius of the nanoparticle cross section at the interface between the PS-rich and P4VP(PDP)₁-rich domains:

$$a = d + 2\Delta a$$

Δa increases with the size of nanoparticles. As shown in **Fig. S12A**, the value of Δa can be calculated via the Pythagorean theorem:

$$\Delta a = \sqrt{r^2 - \left(\frac{l}{2}\right)^2}$$

Where r is the radius of nanoparticles and the l is the width of each P4VP-rich layer. Although this is an oversimplified model, which neglects the nanoparticles' effect on chain morphology and PS/P4VP(PDP)₁ interfaces, it provides us with a rough estimation of the in-plane inter-particle distance as a function of nanoparticle size. Using data obtained from the blend S1/20/PDP(1), where $r = 10.85$ nm, $d = 32$ nm, we see that the width of the

P4VP(PDP)₁-rich layer $l = 10.67$ nm. Then, substituting this l for $r = 6.85$ nm (S1/15/PDP(1)) and $r = 15.85$ nm (S1/30/PDP(1)), the predicted in-plane inter-particle distances are 40.61 nm and 61.85 nm, respectively, which is within 6% of the measurement in **Fig. 3H**.

When comparing the morphology of particle-rich regions and no-particle regions in a PS layer with one row of particles removed, the regions with incorporated particles have a larger hole size. This, in turn, increases the in-plane interparticle distance, as shown in **Fig. S13**.

S7. Hierarchical assembly characterization

The complex blends can form hierarchical assemblies with tunable microstructures and ordered nanostructures. **Fig.S14** shows the solution phase separated into two regions with different concentrations of nanoparticles (**Fig. S14A**). Within the nanoparticle-rich region, there is a characteristic inter-particle distance templated by the supramolecule although the order is poor. Worm-like nanostructures are also seen in the region without nanoparticles (Inset in **Fig. S14B**), confirming nanostructure formation in both phases.

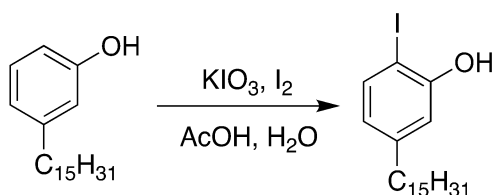
S7.1 Ultra-Small-angle X-ray Scattering (USAXS)

USAXS studies were performed to probe the formation of microstructures. Absolutely-calibrated USAXS and SAXS experiments were collected at beamline 9-ID at APS, Argonne National Laboratory (47). The combined q range is between $1 \times 10^{-4} \text{ \AA}^{-1}$ and 1.3 \AA^{-1} ; here $q = 4\pi/\lambda \sin(\theta)$, λ is the wavelength, and θ is $\frac{1}{2}$ of the scattering angle. The X-ray energy was 21 keV ($\lambda = 0.5895 \text{ \AA}$). X-ray photon flux was $\approx 5 \times 10^{12} \text{ mm}^{-2}\text{s}^{-1}$ through a beam size of $0.5 \times 0.5 \text{ mm}$. Data were reduced using USAXS instrument data

reduction software and were desmeared from slit smeared collimation of the Bonse-Hart USAXS system.

S8. Small molecule synthesis

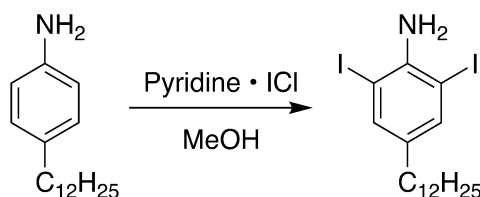
All reactions were carried out in oven-dried glassware sealed with rubber septa under an atmosphere of nitrogen unless otherwise noted and were stirred using Teflon-coated magnetic stir bars. Large volumes of volatile solvents were removed using rotary evaporation, and small volumes of volatile solvents were removed using nitrogen gas flow. All NMR spectra were recorded at 298 K on a Bruker 500 MHz Avance instrument. All chemical shifts are quoted using the δ scale, and all coupling constants (J) are expressed in Hertz (Hz). ^1H and ^{13}C NMR spectra chemical shifts are reported relative to the residual solvent signal (^1H NMR: CDCl_3 $\delta = 7.26$ ppm; ^{13}C NMR: CDCl_3 $\delta = 77.16$ ppm). NMR data are reported as follows: chemical shift (multiplicity, coupling constants where applicable, number of hydrogens where applicable). Splitting is reported with the following symbols: s = singlet, d = doublet, t = triplet, dd = doublet of doublets, q = quartet, m = multiplet.



S8.1 Synthesis of 2-iodo-5-pentadecylphenol (I-PDP)

Iodine-functionalized 3-n-Pentadecylphenol (2-iodo-5-pentadecylphenol, I-PDP) was synthesized from 3-pentadecylphenol in one step via reaction with molecular iodine in the presence of potassium iodate. To a solution of 3-pentadecylphenol (20.00 g, 65.68

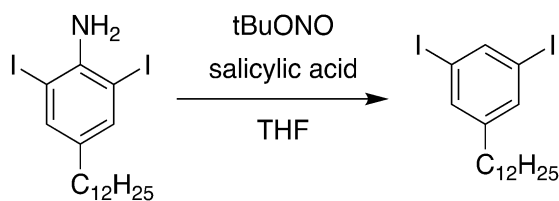
mmol) in glacial acetic acid (200 mL) was added potassium iodate (2.81 g, 13.14 mmol) in water (50 mL) followed by iodine (6.67 g, 26.27 mmol). The mixture was stirred at room temperature for 48 h and then the reaction mixture was filtered. The collected solid was washed with water and thoroughly dried before being purified via column chromatography (eluted with a hexanes/ ethyl acetate gradient) to yield the title compound as a white solid (68%) ^1H NMR (500 MHz, CDCl_3): δ 7.53 (d, $J = 8.1$ Hz, 1H), 6.86 (d, $J = 2.1$ Hz, 1H), 6.53 (dd, $J = 8.1, 2.1$ Hz, 1H), 5.26 (s, 1H), 2.58 – 2.51 (m, 2H), 1.61 (q, $J = 7.4$ Hz, 2H), 1.34 – 1.27 (m, 24H), 0.91 (t, $J = 6.9$ Hz, 3H) (**Fig. S16**). ^{13}C NMR (126 MHz, CDCl_3): δ 154.68, 145.92, 137.85, 123.00, 115.30, 82.01, 77.41, 77.16, 76.91, 35.56, 32.09, 31.26, 29.88, 29.86, 29.84, 29.74, 29.64, 29.54, 29.37, 22.86, 14.30 (**Fig. S17**). The analytic data is in accordance with previously-reported characterization (48).



S8.2 Synthesis of 2,6-Diiodo-4-dodecylaniline

This compound was synthesized via a modified version of a previously reported procedure (49). A 100 mL round-bottom flask equipped with a condenser and a magnetic stir bar was charged with 4-dodecylaniline (1.50 g, 5.74 mmol), pyridinium iodine monochloride (4.16 g, 17.21 mmol), and methanol (30 mL). The reaction mixture was heated to reflux and stirred overnight. The next day, the reaction mixture was filtered and the solid was washed with diethyl ether (30 mL). The filtrate was further purified by being washed through a silica short-plug (eluent: chloroform). The solvent was removed *in vacuo*

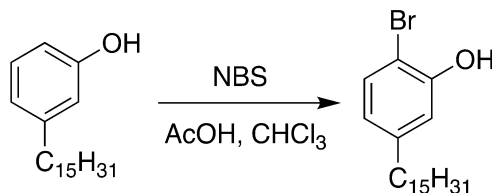
to yield the pure product as a white amorphous solid in quantitative yield. ^1H NMR (500 MHz, CDCl_3) δ 7.45 (s, 2H), 4.45 (s, 2H), 2.40 (dd, $J = 8.7, 6.9$ Hz, 2H), 1.51 (t, $J = 7.6$ Hz, 2H), 1.27 (d, $J = 8.8$ Hz, 18H), 0.89 (t, $J = 6.8$ Hz, 3H) (**Fig.S18**). ^{13}C NMR (126 MHz, CDCl_3) δ 143.90, 139.17, 136.31, 81.60, 33.96, 31.96, 31.54, 29.71, 29.68, 29.59, 29.47, 29.40, 29.15, 22.74, 14.19 (**Fig.S19**).



S8.3 Synthesis of 3,5-Diiodo-dodecylbenzene (DID)

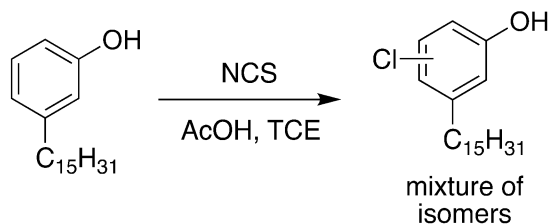
This compound was synthesized via a modified version of a previously reported procedure (50). 2,6-Diiodo-4-dodecylaniline (2.40 g, 4.68 mmol) and a catalytic amount of salicylic acid (64.59 mg, 467.61 μmol) were added to an oven-dried stir bar-equipped 50 mL round-bottom flask under a N_2 atmosphere. Dry THF (24 mL) was added to the flask, and the reaction mixture was stirred vigorously until a homogeneous solution was obtained (approx. 5 min). At this point, tert-butyl nitrite (neat, 0.67 mL, 5.61 mmol) was added and the solution turned orange. The stirring was continued for 3 hours, keeping the temperature at 20°C with a water bath. At this point, the reaction was quenched with H_2O (10 mL) and extracted with ethyl acetate (3 x 10 mL). The organic fractions were dried over anhydrous magnesium sulfate, filtered, and the solvent was removed *in vacuo*. The residue was purified via column chromatography (hexanes to ethyl acetate gradient) to yield pure product in 72% yield as a white amorphous solid. ^1H NMR (500 MHz, CDCl_3) δ 7.85 (d, $J = 1.6$ Hz, 1H), 7.48 (s, 2H), 2.51 – 2.44 (m, 2H), 1.55 (q, $J = 7.6, 5.4$ Hz, 2H),

1.27 (d, $J = 15.2$ Hz, 18H), 0.88 (t, $J = 6.8$ Hz, 3H) (Fig. S20). ^{13}C NMR (126 MHz, CDCl_3) δ 147.37, 142.39, 136.92, 94.88, 35.28, 32.07, 31.26, 29.81, 29.79, 29.78, 29.66, 29.53, 29.51, 29.29, 22.86, 14.31 (Fig. S21).



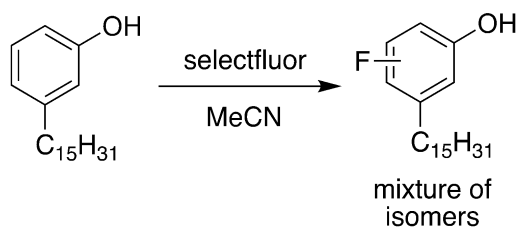
S8.4 Synthesis of 2-bromo-5-pentadecylphenol (Br-PDP)

In a stir bar-equipped, aluminum foil-wrapped, 200 mL round-bottom flask, 3-pentadecylphenol (5.00 g, 16.42 mmol) was added to a mixture of CHCl_3 (100 mL) and acetic acid (190 μL , 3.28 mmol). N-bromosuccinimide (3.07 g, 17.24 mmol) was then added and the mixture was stirred in the dark at room temperature for 72 hours. Afterwards, the solvent was evaporated *in vacuo* and the residue was purified via flash chromatography (hexanes to ethyl acetate gradient) to yield a white powder in 67% yield (not including the other isomers generated, which could be separated from the main product). ^1H NMR (500 MHz, CDCl_3) δ 7.35 (d, $J = 8.6$ Hz, 1H), 6.71 (s, 1H), 6.55 (d, $J = 8.7$ Hz, 1H), 5.16 (bs, 1H), 2.64 (t, $J = 7.8$ Hz, 2H), 1.59 (p, $J = 7.5$ Hz, 2H), 1.27 (m, 24H), 0.89 (t, $J = 7.0$ Hz, 3H) (Fig. S22).



S8.5 Synthesis of monochloro-pentadecylphenol (mixture of isomers) (Cl-PDP)

In a stir bar-equipped, aluminum foil-wrapped, 200 mL round-bottom flask with a condenser, 3-pentadecylphenol (5.00 g, 16.42 mmol) was added to a mixture of 1,1,2-trichloroethylene (100 mL) and acetic acid (940 μ L, 16.42 mmol). N-chlorosuccinimide (2.30 g, 17.24 mmol) was then added and the mixture was stirred at 90 °C for 72 hours in the dark. Afterwards, the solvent was evaporated *in vacuo* and the residue was purified via flash chromatography (hexanes to ethyl acetate gradient) to yield 73% of a mixture of the isomers of monochloro-pentadecylphenol.



S8.6 Synthesis of monofluoro-pentadecylphenol (mixture of isomers) (F-PDP)

In a stir bar-equipped, 200 mL round-bottom flask with a condenser, 3-pentadecylphenol (3.00 g, 9.85 mmol) was dissolved in acetonitrile (60 mL). Selectfluor® (3.49 g, 9.85 mmol) was then added and the mixture was stirred at 85 °C for 24 hours. Afterwards, the mixture was diluted with ethyl acetate (50 mL) and sequentially washed with water (50 mL) and brine (50 mL). Drying over anhydrous magnesium sulfate followed by filtration and concentration provided a residue that was purified by silica gel chromatography (hexanes to ethyl acetate gradient) to yield 91% of a mixture of the isomers of monofluoro-pentadecylphenol.

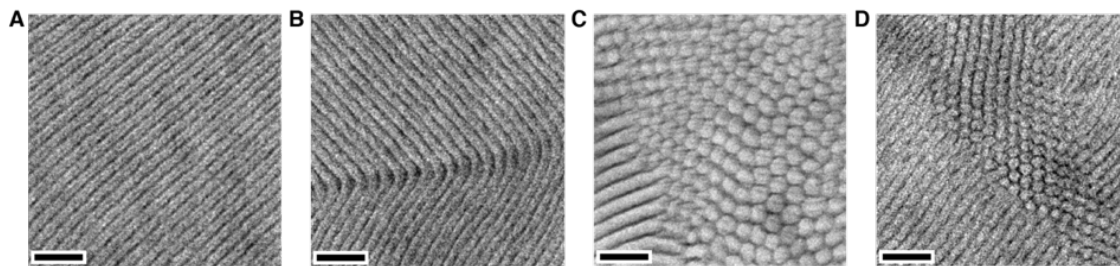


Fig. S1. TEM images of blends of supramolecule PS-*b*-P4VP(PDP)₁ and small molecules. The blends use the following notation: supramolecule/small molecules (molar ratio to 4VP). **A**, S1, lamellae morphology. **B**, S1/PDP (0.5) lamellae morphology. **C**, S1/PDP (1), cylindrical morphology. **D**, S2/PDP (1.5), cylindrical morphology. Scale bar: 100 nm. S1: P4VP (33 kDa)-*b*-PS (8 kDa)PDP₁; S2: P4VP (19 kDa)-*b*-PS (5.2 kDa)PDP₁.
Scale bar: 100 nm.

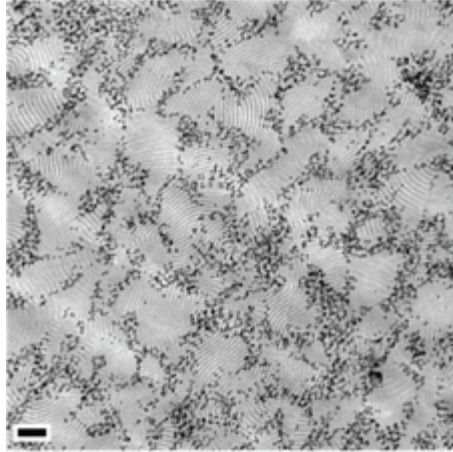


Fig. S2. TEM images of the blend without free small molecules. The blend composition is S1/20 nm. Nanoparticles aggregate at grain boundaries and defect regions in blends without free small molecules. Similar results were seen in nanocomposites containing nanoparticles with different core chemistries. **Scale bar:** 200 nm.

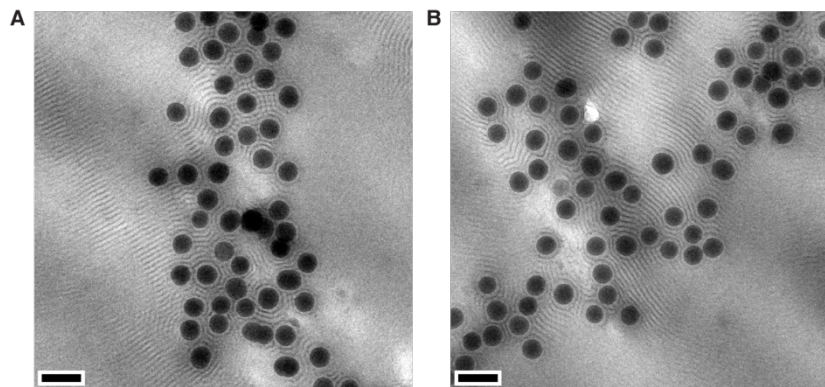


Fig. S3. Assemblies of complex blends containing 100 nm colloidal particles. Two representative TEM images of C14 (S1/100/DID(1)). **A** is the Low-magnification image of the morphology shown in **Fig. 2B**. The colloidal particles can be solubilized in the complex blends, and the soft matrix locally adjusts to accommodate colloidal particles. **Scale bars:** 200nm.

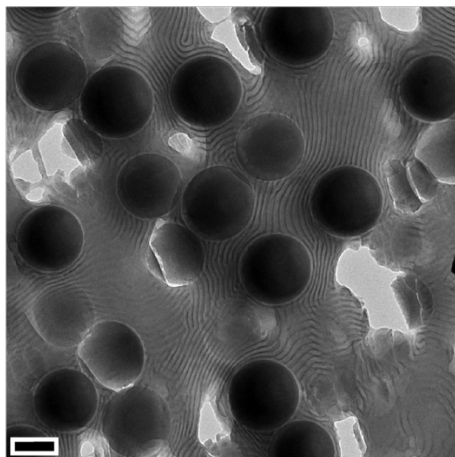


Fig. S4. Assemblies of complex blends containing 300 nm colloidal particles. TEM image of S1/300/DID(2). 300 nm particles are well dispersed in the nanostructured matrix.
Scale bars: 200 nm.

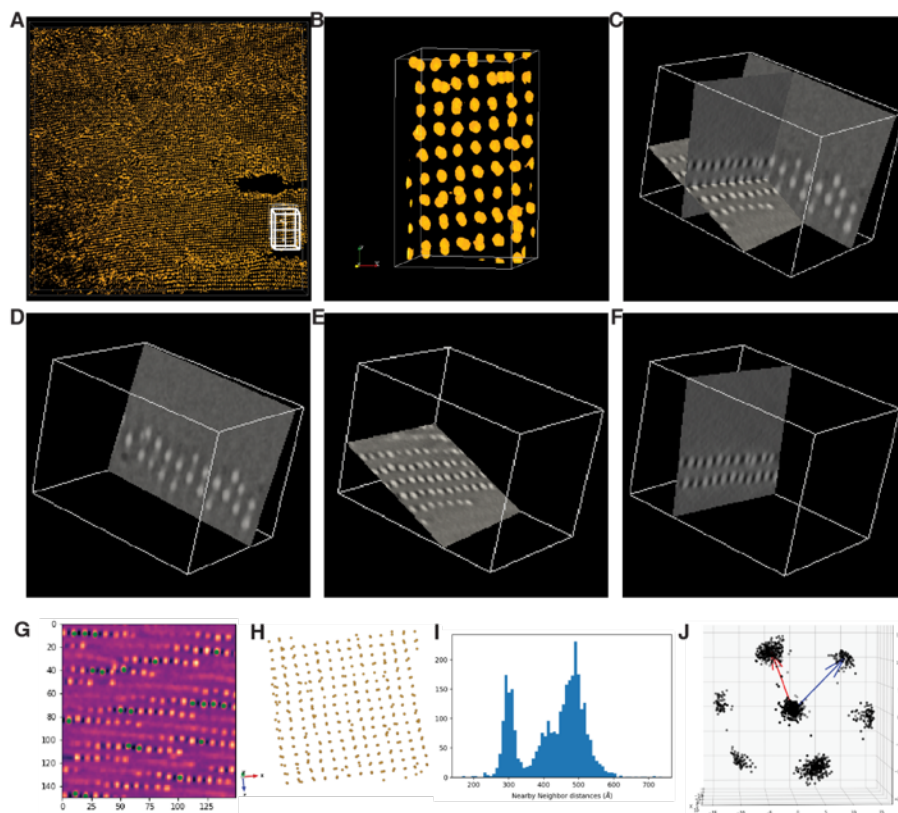


Fig. S5. STEM tomography reconstruction and unit cell analysis of C1 (S1/20/PDP(1)). **A**, Full reconstruction morphology. **B**, One projection of the morphology labeled by the white box in **A** (see also **Movie S1**). **C-F**, Three slices of the tomographic reconstruction, white dots are nanoparticles. **D**, Hexagonal nanoparticle lattice. **E, F**, Square nanoparticle lattice. **G**, One slice of the reconstruction; green spots represent nanoparticles in the particular layer. **H**, 3-D plot of nanoparticle positions. **I**, The distribution of the distances between neighboring particles. **J**, Lattice unit cell (see also **Movie S2**).

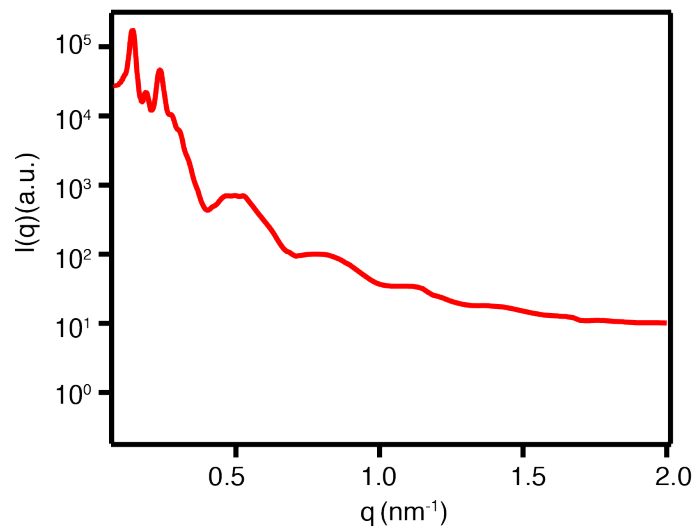


Fig. S6. 1D circularly-averaged SAXS profiles of C1 (S1/20/PDP(1)).

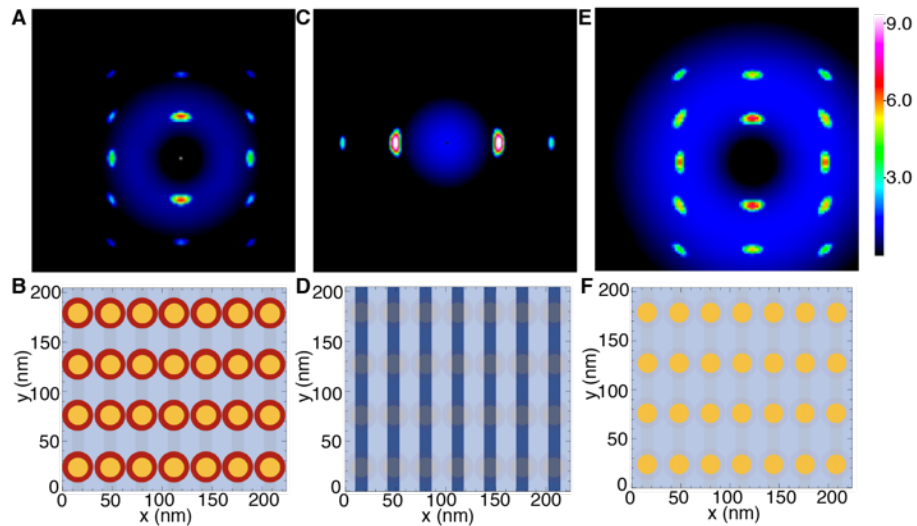


Fig. S7. Simulated RSoXS diffraction patterns and corresponding simulation models.

A, B, The simulated diffraction pattern from the model shown in **B**, where the core and shell have large contrast. **E, D**, The simulated diffraction pattern from the lamellar model shown in **D**, taken around the carbon edge 285 eV. **E, F**, the simulated diffraction pattern from the model shown in **F**, where the shell's effective electron density matches that of the matrix.

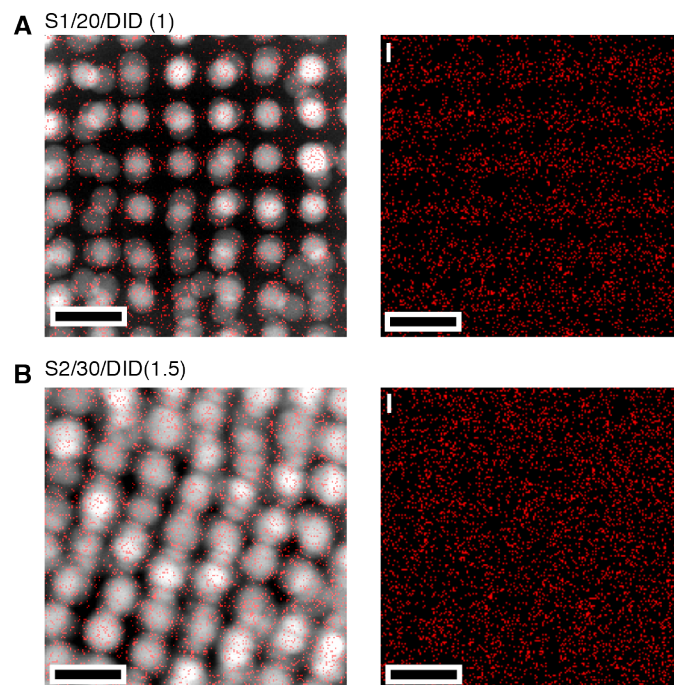


Fig.S8. Small molecule distribution in different complex blends. A, STEM-EDS maps of iodine-labelled small molecules in S1/20/DID(1). **B,** STEM-EDS maps of iodine-labelled small molecules in S2/30/DID(1.5). **Scale bars:** 50 nm.

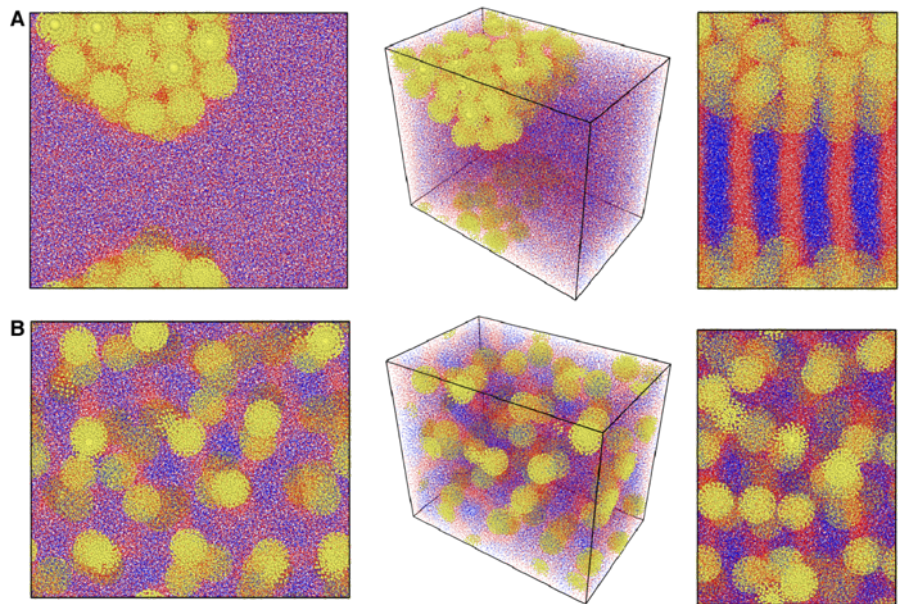


Fig. S9. DPD simulation results of complex blends with various intermolecular interactions. **A**, Results from a simulation where the nanoparticle/PDP interaction force is neutral. Without a favorable interaction between the small molecules and nanoparticles, the ordered particle arrangement is not maintained. **B**, Results from a simulation where neither polymer block has a comb architecture. Without this architecture, the nanoparticles do not experience long-range repulsion within the lamellar domains. The assembly includes phase-separated nanoparticle aggregates.

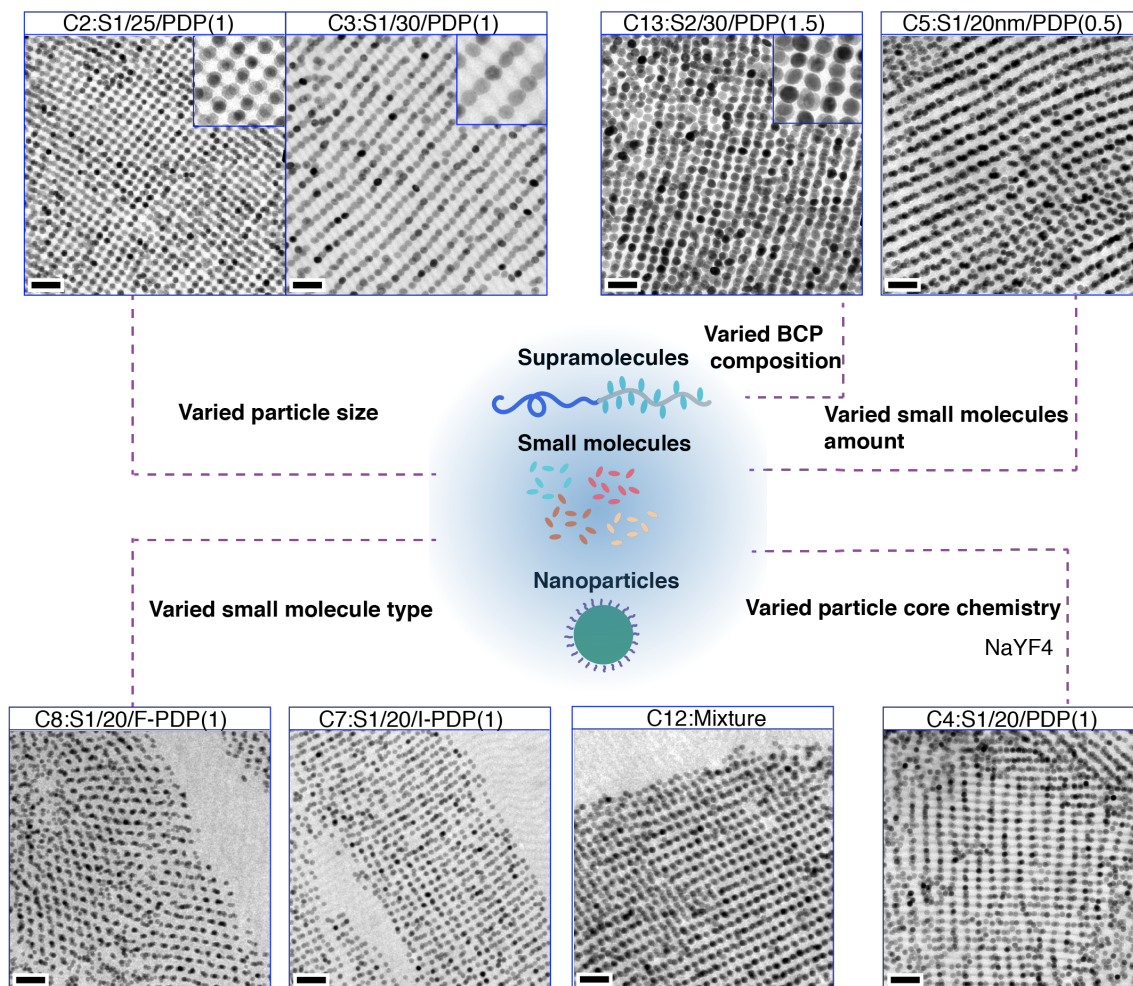


Fig. S10. Formulation flexibility in complex blends. TEM images of complex blends with various compositions. The blends are able to accommodate many formulation variations without compromising the precision of the nanoscopic assemblies. **Scale bars:** 100 nm. Inset TEM images are 150 nm x 150 nm in size.

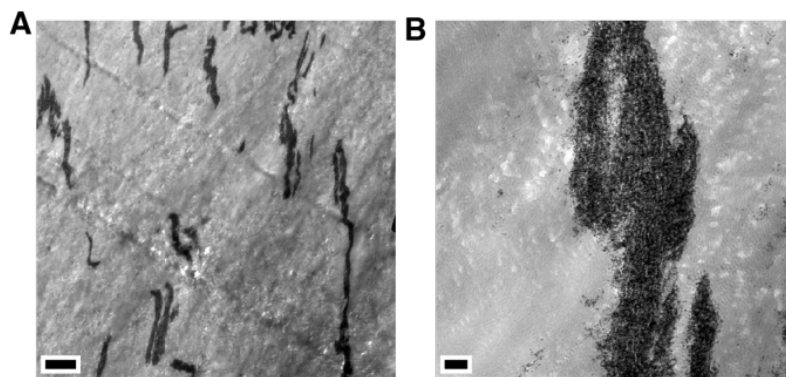


Fig. S11. TEM images of S1/20/DDSA. When the small molecule solubility parameter is not within the allowable range, the nanoparticles form aggregates. **Scale bar:** 200 nm.

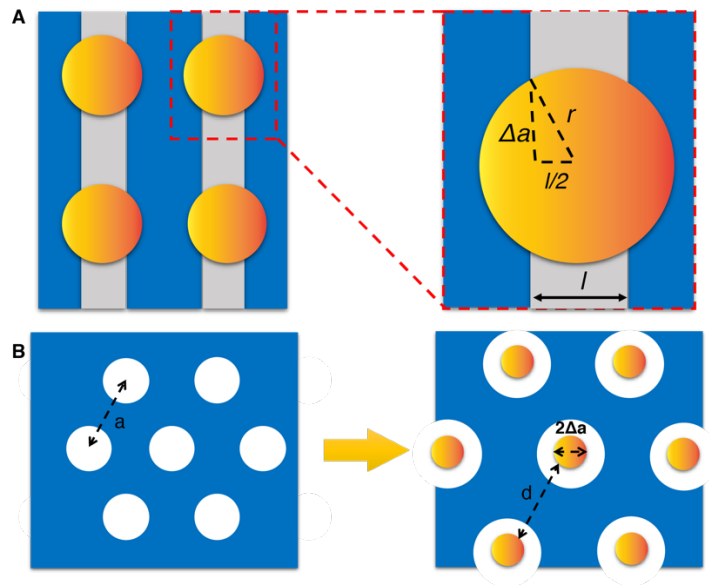


Fig. S12. In-plane interparticle distance calculation. Blue: PS-rich block; Gray: P4VP(PDP)₁-rich block; Yellow: nanoparticles.

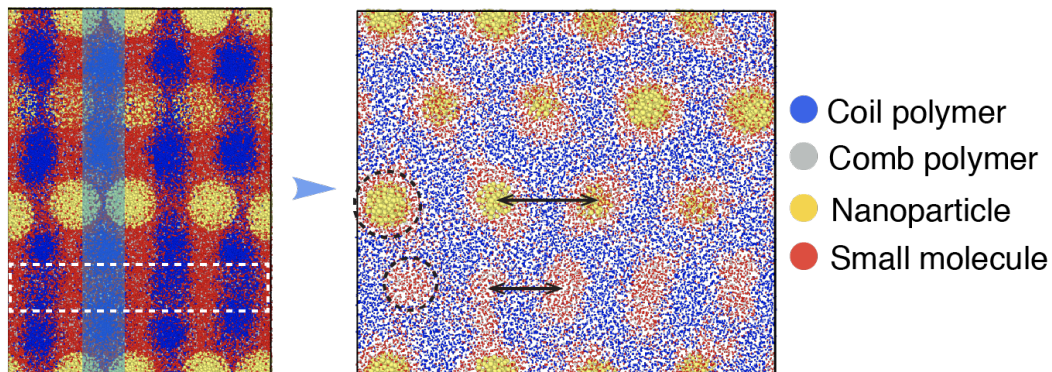


Fig. S13. DPD simulation results of a complex blend with one row of particles removed. The white box in the left image shows the position of removed particles. The right image shows the morphology of the top view of a coil polymer layer, labeled by blue box in the left image. The incorporation of particles enlarges the hole size, which in turn increases the in-plane interparticle distance.

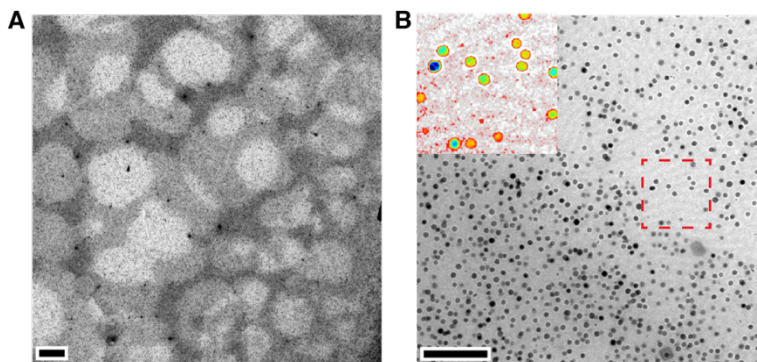


Fig. S14. TEM images of drop-cast C1(S1/20/PDP(1)) solution trapped in a TEM liquid cell. The solution phase separated into two regions with different concentrations of nanoparticles. The dark regions have higher particle concentrations, while the gray regions have lower particle concentrations. The inset in **B** is the color-coded image of the red box region. **Scale bar:** 200 nm.

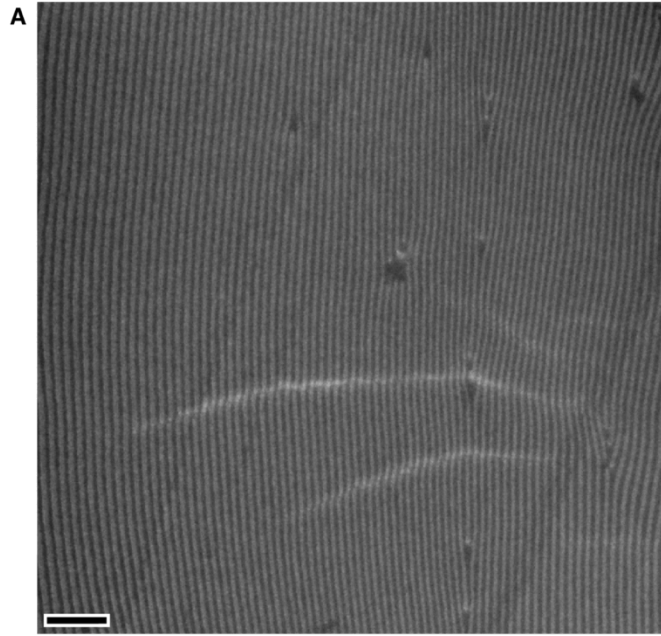


Fig. S15. Low-magnification image of the photonic crystal shown in **Fig. 3B** and **3C**. **Scale bar:** 1 μm .

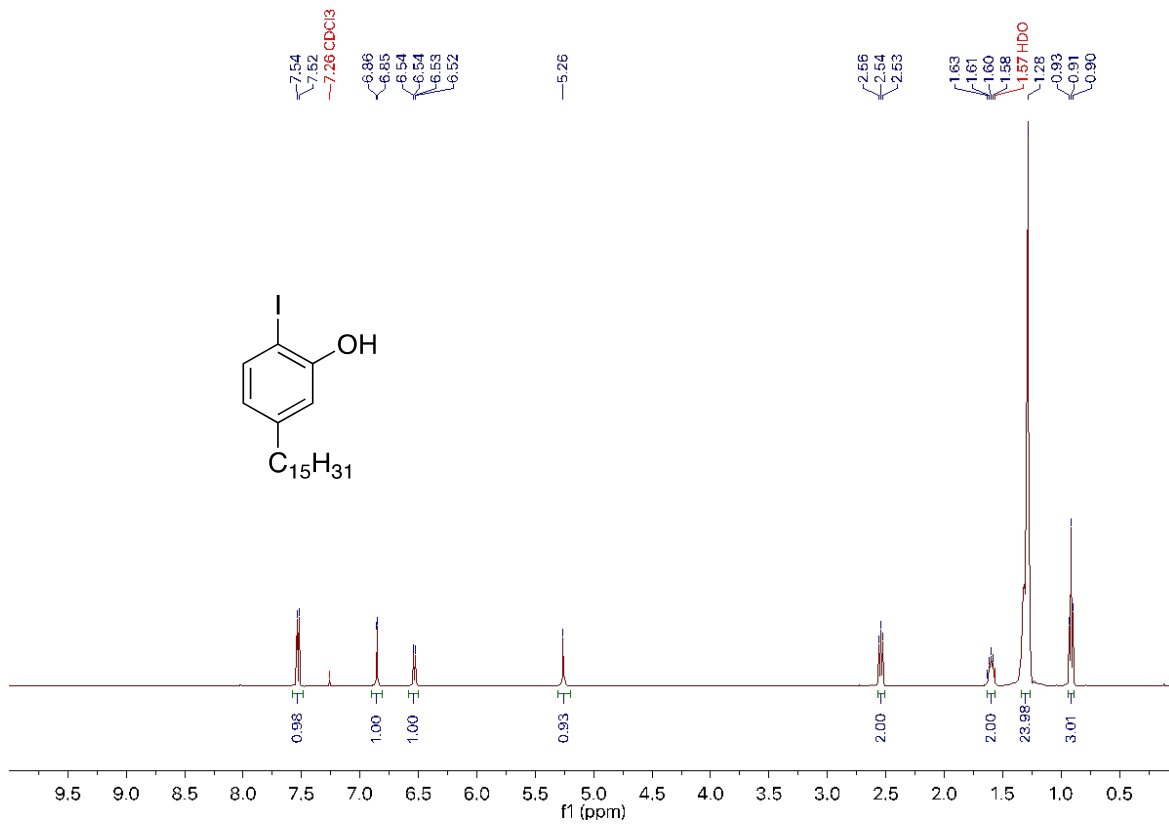


Fig.S16. $^1\text{H-NMR}$ spectrum of 2-iodo-5-pentadecylphenol (I-PDP) (CDCl₃, 298K).

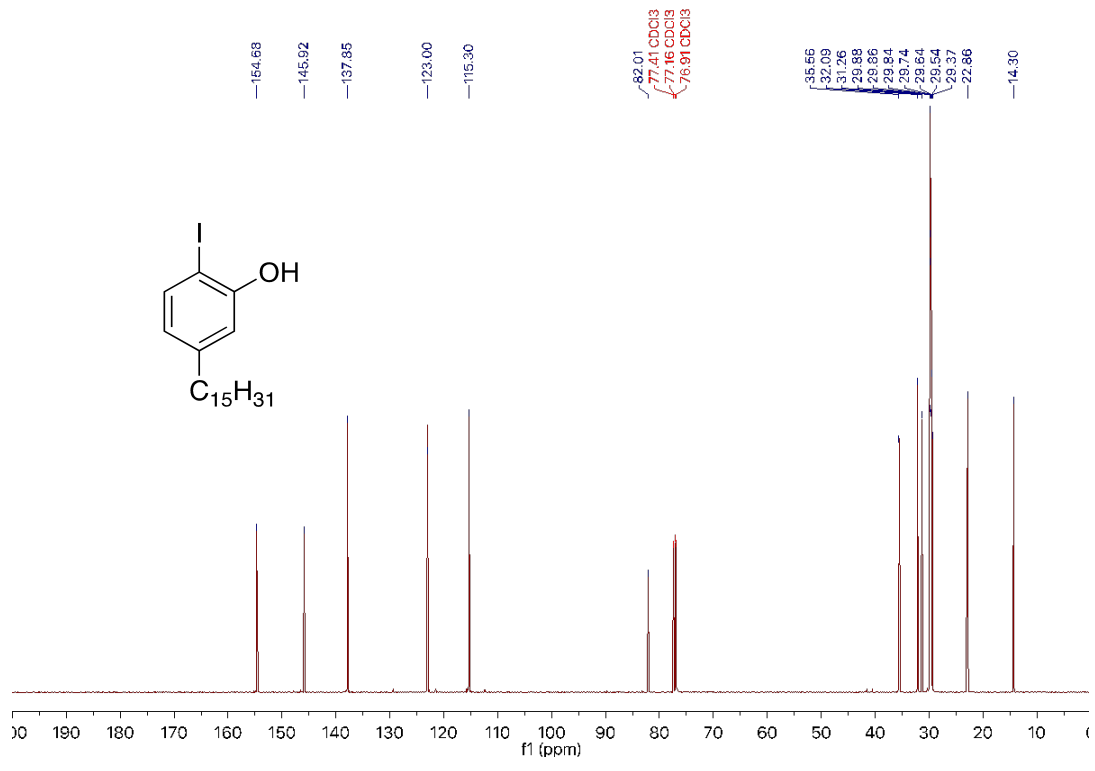


Fig. S17. ^{13}C -NMR spectrum of 2-iodo-5-pentadecylphenol (I-PDP) (CDCl_3 , 298K).

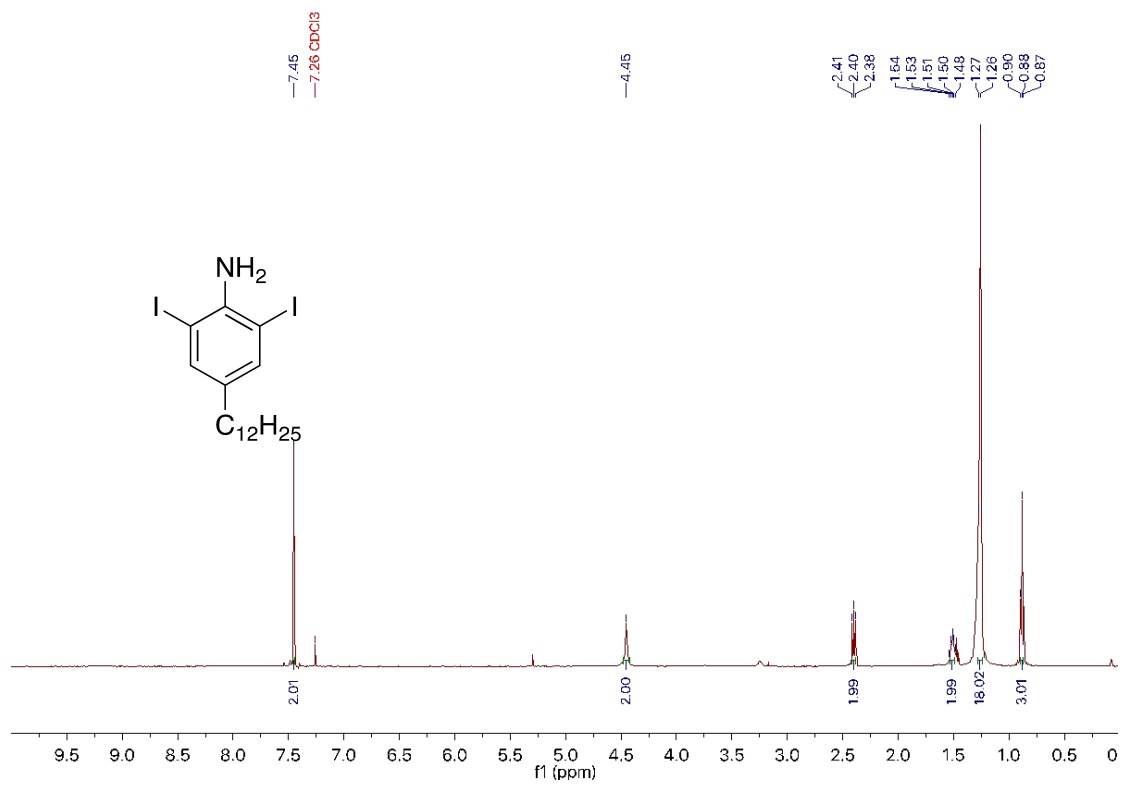


Fig. S18. ¹H-NMR spectrum of 2,6-Diiodo-4-dodecylaniline (CDCl₃, 298K).

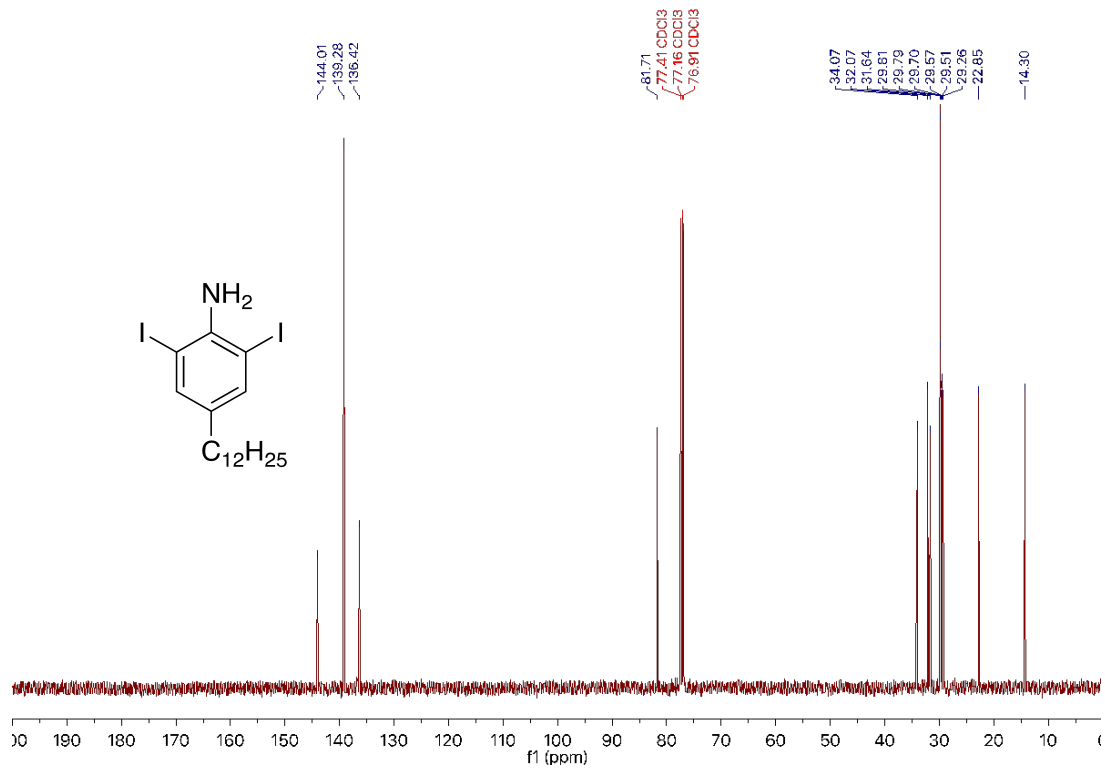


Fig. S19. ^{13}C -NMR spectrum of 2,6-Diiodo-4-dodecylaniline (CDCl_3 , 298K).

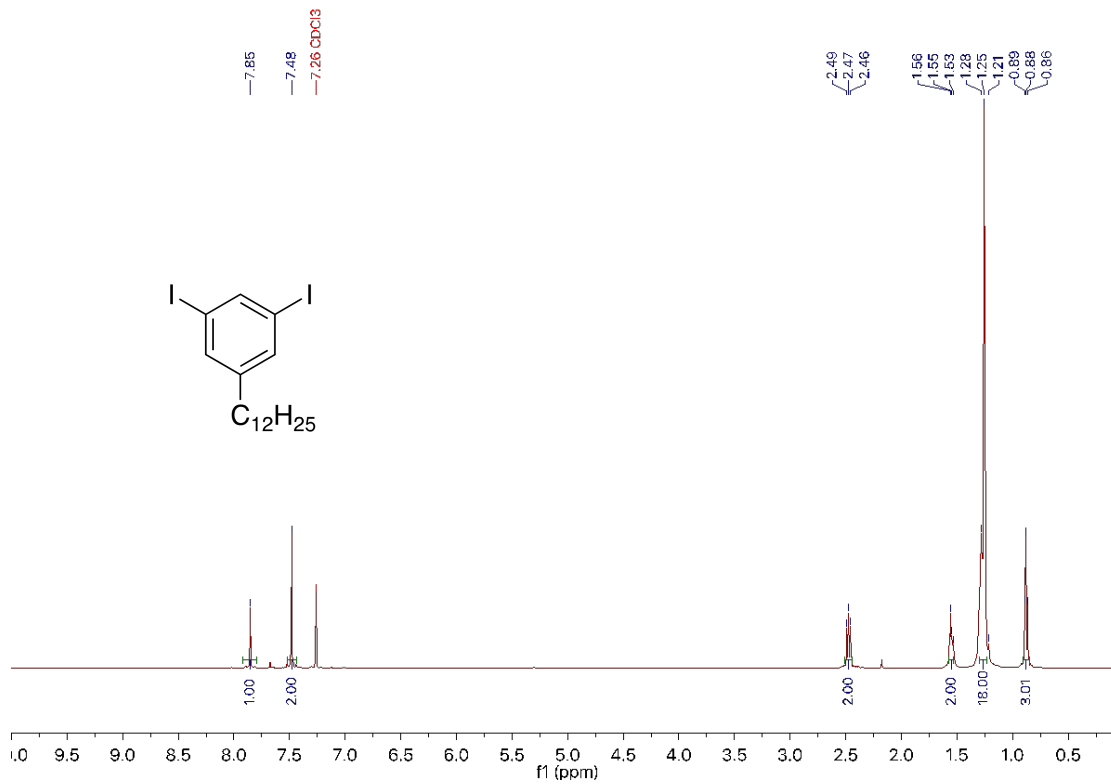


Fig. S20. ¹H-NMR spectrum of 3,5-Diiodo-dodecylbenzene (DID) (CDCl₃, 298K).

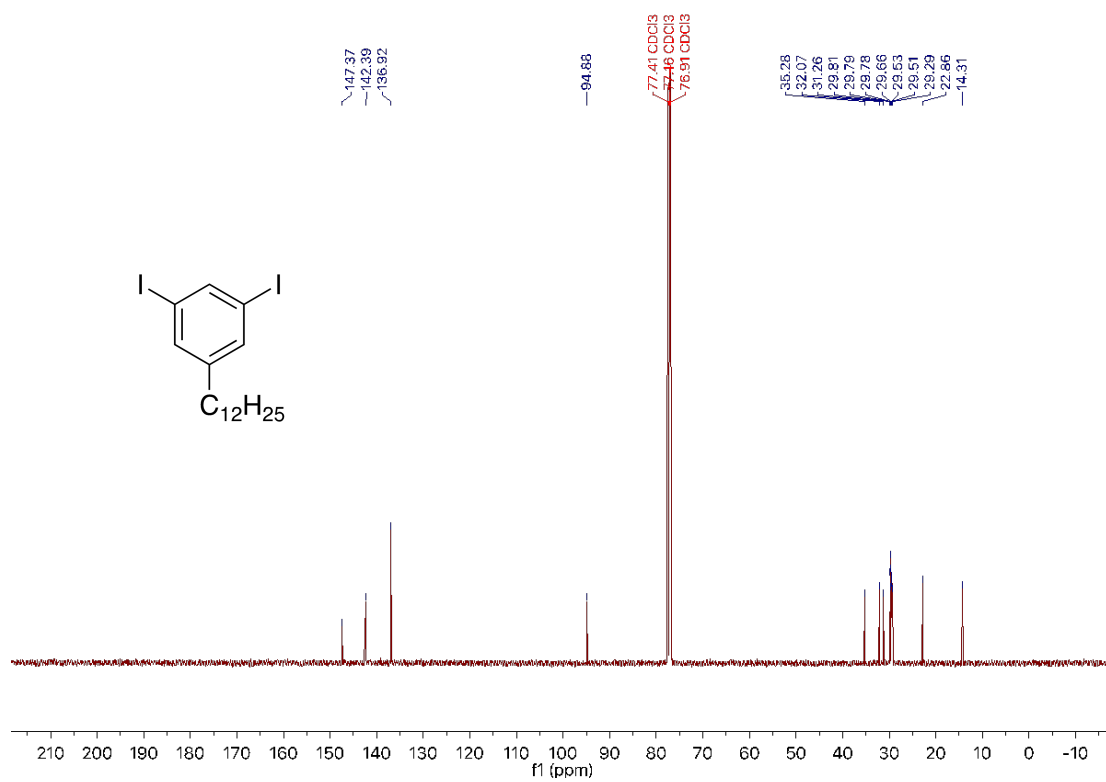


Fig. S21. ^{13}C -NMR spectrum of 3,5-Diiodo-dodecylbenzene (DID) (CDCl_3 , 298K).

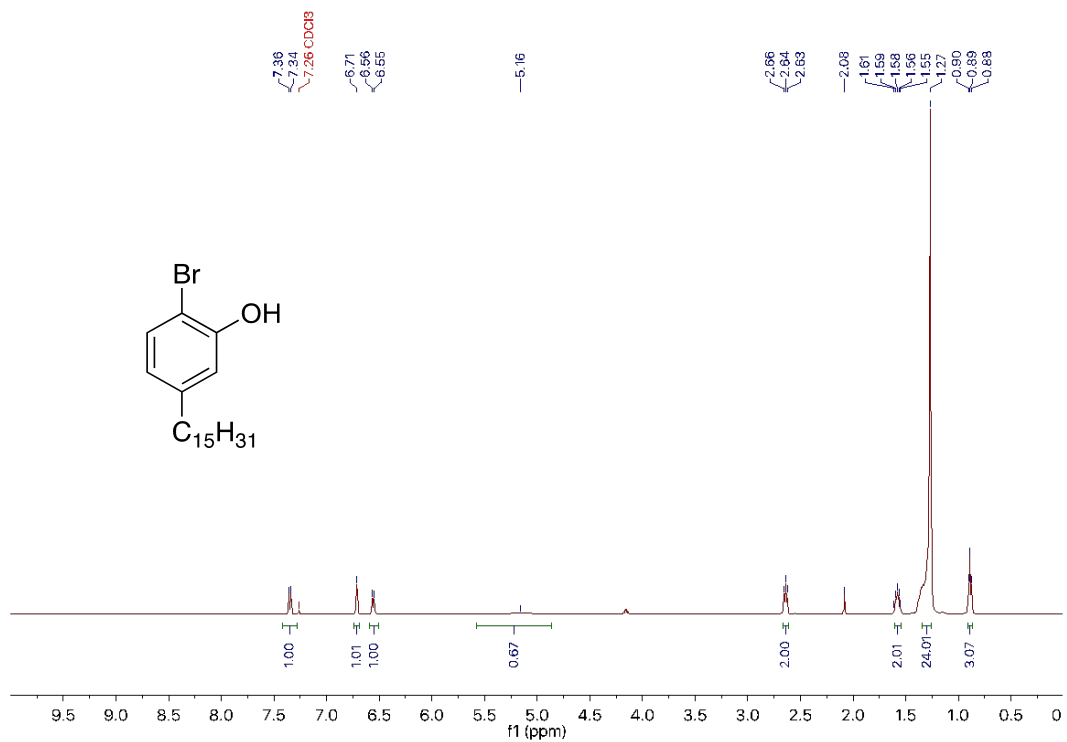


Fig. S22. ¹H-NMR spectrum of 2-bromo-5-pentadecylphenol (Br-PDP) (CDCl₃, 298K).

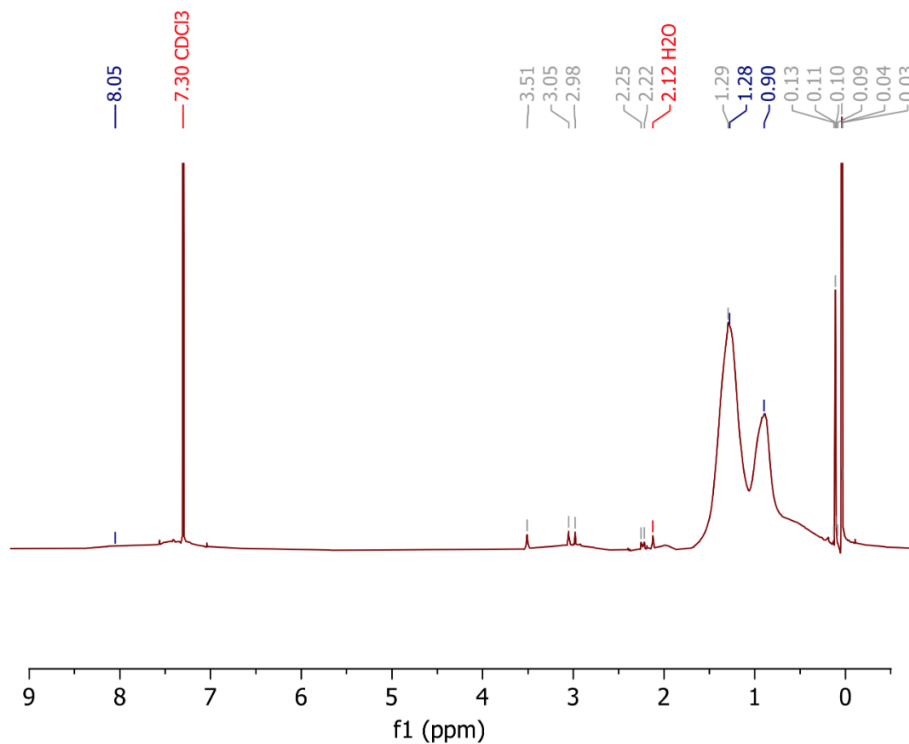


Fig. S23. ¹H-NMR spectrum of commercial ZrO₂ nanoparticles with unknown ligand chemistry (CDCl₃, 298K). The exact ligand chemistry is a trade secret, but the NMR results are consistent with an alkyl chain.

Table S1. Blend Composition Details

Blend	Supramolecule	Nanoparticle	Small molecules (weight fraction, molar ratio to 4VP)
C1	S1	Fe ₃ O ₄ , 20 nm	PDP (27 wt%, 1)
C2	S1	Fe ₃ O ₄ , 25 nm	PDP (27 wt%, 1)
C3	S1	Fe ₃ O ₄ , 30 nm	PDP (27 wt%, 1)
C4	S1	NaYF ₄ , 20 nm	PDP (27 wt%, 1)
C5	S1	Fe ₃ O ₄ , 20 nm	PDP (15 wt%, 0.5)
C6	S1	Fe ₃ O ₄ , 20 nm	DID (37 wt%, 1)
C7	S1	Fe ₃ O ₄ , 20 nm	I-PDP (34 wt%, 1)
C8	S1	Fe ₃ O ₄ , 20 nm	F-PDP isomer mixture (28 wt%, 1)
C9	S1	Fe ₃ O ₄ , 20 nm	Cl-PDP isomer mixture (29 wt%, 1)
C10	S1	Fe ₃ O ₄ , 20 nm	Br-PDP (31 wt%, 1)
C11	S1	Fe ₃ O ₄ , 20 nm	DDMA (27 wt%, 1)
C12	S1	Fe ₃ O ₄ , 20 nm	DID (17 wt%, 0.5) + F-PDP (11 wt%, 0.5) + I-PDP (14 wt%, 0.5)
C13	S2	Fe ₃ O ₄ , 30 nm	PDP (37 wt%, 1.5)
C14	S1	PS grafted silica nanoparticle, 100 nm	DID (54 wt%, 2)
C15	S3	ZrO ₂ , 6 nm	PDP (21 wt%, 0.6)

S1: PS (33 kDa)-*b*-P4VP (8 kDa)PDP₁;

S2: PS (19 kDa)-*b*-P4VP (5.2 kDa)PDP₁;

S3: PS (330 kDa)-*b*-P4VP (125 kDa)PDP₁;

PDP: 3-pentadecyl phenol;

DID: 3,5-Diiodo-dodecylbenzene;

I-PDP: 2-iodo-5-pentadecylphenol;

F-PDP: monofluoro-pentadecylphenol;

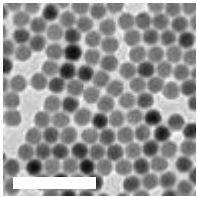
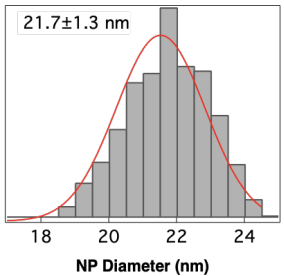
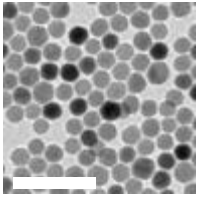
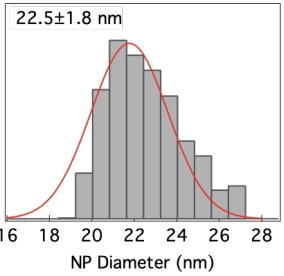
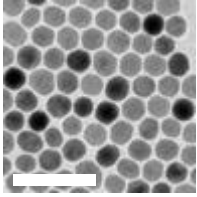
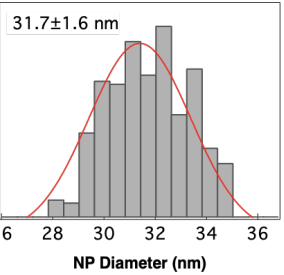
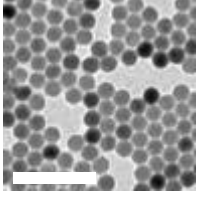
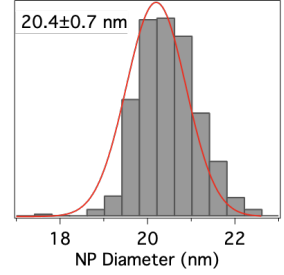
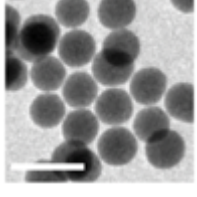
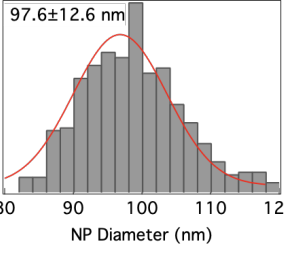
Cl-PDP: monochloro-pentadecylphenol;

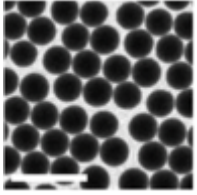
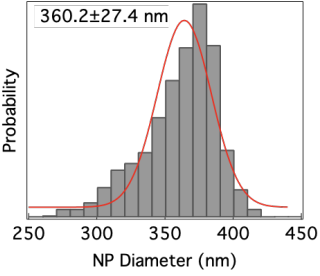
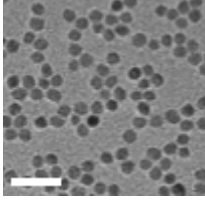
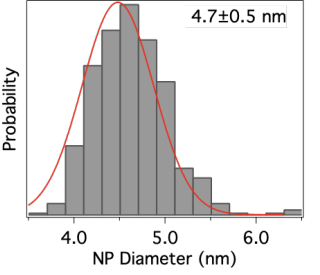
Br-PDP: 2-bromo-5-pentadecylphenol;

DDMA: 1,10-Decanediol dimethacrylate.

weight fraction of small molecule = mass of small molecules / (mass of supramolecule + mass of small molecules)

Table S2. Particle information

Type	ligand	Size (nm)	TEM image	Size distribution
Iron oxide (Fe ₃ O ₄)	Oleic acid	20	 <p>Scale bar: 100 nm</p>	 <p>21.7±1.3 nm</p>
Iron oxide (Fe ₃ O ₄)	Oleic acid	25	 <p>Scale bar: 100 nm.</p>	 <p>22.5±1.8 nm</p>
Iron oxide (Fe ₃ O ₄)	Oleic acid	30	 <p>Scale bar: 100 nm.</p>	 <p>31.7±1.6 nm</p>
Up-conversion nanoparticle (NaYF ₄)	Oleic acid	20	 <p>Scale bar: 100 nm.</p>	 <p>20.4±0.7 nm</p>
PS-grafted silica nanoparticle	PS	100	 <p>Scale bar: 200nm</p>	 <p>97.6±12.6 nm</p>

PS-grafted silica nanoparticle	PS	360	 <p>Scale bar: 1 μm</p>	 <p>360.2 \pm 27.4 nm</p>
Zirconium oxide (ZrO ₂) nanoparticle	alkyl chains (see NMR in Fig. S24)	4-6	 <p>Scale bar: 20 nm</p>	 <p>4.7 \pm 0.5 nm</p>

NP: nanoparticle.

Table S3. The DPD simulation interaction parameters between different components

a_{ij}	Interaction parameter	χ^N
a_{AB}	34.6	270
a_{AC}	30.0	0
a_{AD}	≤ 15.0	Negative (attractive interactions)
a_{BC}	35.8	40
a_{BD}	16.4 ~ 17.9	20 ~ 40
a_{CC}	30.0	0
a_{CD}	≤ 20.0	Negative (attractive interactions)

A B C and D, which represents comb polymer (P4VP), coil polymer (PS), nanoparticle, and small molecule, respectively.

Table S4. Lattice parameters as a function of particle size and supramolecule type

Blends	NP size (nm)	<i>a</i> (nm)	<i>c</i> (nm)
S1/Nanoparticles/PDP(1)	13.7	43.1 ± 1.1	31.7 ± 1.8
	21.7	50.9 ± 1.4	32.1 ± 1.1
	31.7	58.0 ± 1.6	32.0 ± 1.4
S2/Nanoparticles/PDP(1.5)	21.7	39.3 ± 1.8	25.6 ± 1.2
	22.5	41.9 ± 0.8	25.6 ± 1.5
	31.7	50.3 ± 2.0	33.0 ± 1.7

S1: P4VP (33 kDa)-*b*-PS (8 kDa)PDP₁;

S2: P4VP (19 kDa)-*b*-PS (5.2 kDa)PDP₁.

Table S5. Lattice parameters as a function of small molecules type and amounts

Blends	<i>a</i> (nm)	<i>c</i> (nm)
S1/20/PDP(0.5)	47.0 ± 1.6	31.9 ± 2.0
S1/20/PDP(1)	50.8 ± 1.4	32.1 ± 1.1
S1/20/PDP(2)	48.4 ± 2.6	32.0 ± 1.4
S1/20/DID(1)	51.9 ± 2.3	31.9 ± 0.9
S1/20/F-PDP(1)	51.5 ± 1.3	N/A
S1/20/Cl-PDP(1)	51.3 ± 1.6	N/A
S1/20/Br-PDP(1)	52.9 ± 2.5	31.7 ± 1.2
S1/20/I-PDP(1)	53.4 ± 1.5	32.7 ± 0.9
S1/20/DID(0.5)/F-PDP(0.5)/I-PDP(0.5)	52.1 ± 0.9	31.3 ± 1.3

Table S6. Flory-Huggins parameters between small molecules and polymers

Small molecules	$\chi_{\text{small molecule/A}}$	$\chi_{\text{small molecule/B}}$
PDP	0.49	0.09
F-PDP	0.37	0.06
Cl-PDP	0.32	0.15
Br-PDP	0.39	0.04
I-PDP	0.41	0.16
DID	0.18	0.26
DDMA	0.5	0.14
DDSA	1.29	0.59

A: PS; B:P4VP(PDP)₁;

$\chi_{i/j}$ is the Flory-Huggins parameters between i and j;

$\chi_{A/B} = 0.52$.

Movie S1. The tomography reconstruction results of the 3-D nanoparticle lattice of C1 (S1/20/PDP(1)). See also **Fig. S5**.

Movie S2 (A, B). The nanoparticle unit cell lattice of C1 (S1/20/PDP(1)). **(A)** In-plane projection. **(B)** Out-of-plane projection. See also **Fig. S5**.

Movie S3. The DPD simulation results of nanoparticle arrangement after release from an initial hexagonal lattice in the complex blend. blue: coil polymer (PS); gray: comb polymer(P4VP); yellow: nanoparticle; red: PDP.

Movie S4. The DPD simulation result of nanoparticle arrangement after release from an initial rectangular lattice in the complex blend. blue: coil polymer (PS); gray: comb polymer(P4VP); yellow: nanoparticle; red: PDP.